














Interferon-inducible phospholipids govern IFITM3-dependent endosomal antiviral immunity

Giulia Unali^{1,2}, Giovanni Crivicich^{1,†}, Isabel Pagani^{3,†} , Monah Abou-Alezz¹ , Filippo Folchini¹, Erika Valeri^{1,2}, Vittoria Matafora⁴ , Julie A Reisz⁵, Anna Maria Sole Giordano¹, Ivan Cuccovillo¹ , Giacomo M Butta^{6,7}, Lorena Donnici⁶ , Angelo D'Alessandro⁵ , Raffaele De Francesco^{6,7} , Lara Manganaro^{6,7}, Davide Cittaro⁸ , Ivan Merelli¹, Carolina Petrillo¹, Angela Bachi⁴ , Elisa Vicenzi¹  & Anna Kajaste-Rudnitski^{1,*} 

Abstract

The interferon-induced transmembrane proteins (IFITM) are implicated in several biological processes, including antiviral defense, but their modes of action remain debated. Here, taking advantage of pseudotyped viral entry assays and replicating viruses, we uncover the requirement of host co-factors for endosomal antiviral inhibition through high-throughput proteomics and lipidomics in cellular models of IFITM restriction. Unlike plasma membrane (PM)-localized IFITM restriction that targets infectious SARS-CoV2 and other PM-fusing viral envelopes, inhibition of endosomal viral entry depends on lysines within the conserved IFITM intracellular loop. These residues recruit Phosphatidylinositol 3,4,5-trisphosphate (PIP3) that we show here to be required for endosomal IFITM activity. We identify PIP3 as an interferon-inducible phospholipid that acts as a rheostat for endosomal antiviral immunity. PIP3 levels correlated with the potency of endosomal IFITM restriction and exogenous PIP3 enhanced inhibition of endocytic viruses, including the recent SARS-CoV2 Omicron variant. Together, our results identify PIP3 as a critical regulator of endosomal IFITM restriction linking it to the PI3K/Akt/mTORC pathway and elucidate cell-compartment-specific antiviral mechanisms with potential relevance for the development of broadly acting antiviral strategies.

Keywords IFITM; innate immunity; phosphatidylinositol 3,4,5-trisphosphate (PIP3); SARS-CoV2; viral entry

Subject Categories Immunology; Membrane & Trafficking; Microbiology, Virology & Host Pathogen Interaction

DOI 10.15252/emboj.2022112234 | Received 27 July 2022 | Revised 27 February 2023 | Accepted 6 March 2023

The EMBO Journal (2023) e112234

Introduction

The interferon-induced transmembrane proteins (IFITM) are a family of small proteins that are involved in the inhibition of a wide spectrum of viruses (Bailey *et al*, 2014; Zhao *et al*, 2018a). IFITM are also gaining relevance in the context of several biological processes as they have been implicated in cancer progression (Liu *et al*, 2019; Lee *et al*, 2020; Rajapaksa *et al*, 2020) placental abnormalities (Buchrieser *et al*, 2019) and we have recently shown that IFITM3 potently blocks viral gene therapy vectors in hematopoietic stem cells (Petrillo *et al*, 2018).

Although our understanding of IFITM antiviral activity has greatly improved, there is still no consensus regarding their precise mechanisms of action that may differ depending on the target cell and virus. IFITM inhibit infection at early stages, impeding viral entry into the host cells (Bailey *et al*, 2014; Smith *et al*, 2014). This is thought to occur via IFITM-mediated changes in the physical properties of the host cell membranes that include increasing curvature, decreasing fluidity and altering membrane composition, thus inhibiting virus-cell membrane fusion (Lu *et al*, 2011; Amini-Bavil-Olyae *et al*, 2013; Li *et al*, 2013; Tartour *et al*, 2017; Suddala *et al*, 2019). Incorporation of IFITM proteins into viral particles may also amplify restriction (Compton *et al*, 2014; Yu *et al*, 2015; Tartour *et al*, 2017), and IFITM1-3 expression reduces viral particle production from cells (Tartour *et al*, 2017; Zhao *et al*, 2018a). In addition, IFITM have been described to suppress HIV-1 protein synthesis by impeding viral mRNA transcription in the polysomes (Lee *et al*, 2018).

Several studies suggest a type IV transmembrane protein topology for IFITM3, consisting of five domains: a N-terminal domain facing the cytoplasm, an intramembrane domain (IMD), a conserved

1 San Raffaele Telethon Institute for Gene Therapy (SR-TIGET), IRCCS Ospedale San Raffaele, Milan, Italy

2 Vita-Salute San Raffaele University, Milan, Italy

3 Viral Pathogenesis and Biosafety Unit, IRCCS Ospedale San Raffaele, Milan, Italy

4 FIRC Institute of Molecular Oncology (IFOM), Milan, Italy

5 Department of Biochemistry and Molecular Genetics, University of Colorado Anschutz Medical Campus, Aurora, CO, USA

6 INGM, Istituto Nazionale Genetica Molecolare "Romeo ed Enrica Invernizzi", Milan, Italy

7 Department of Pharmacological and Biomolecular Sciences (DiSFeB), University of Milan, Milan, Italy

8 Center for Omics Sciences, IRCCS Ospedale San Raffaele, Milan, Italy

*Corresponding author. Tel: +39 0226435007; Fax: +39 0226434668/4621; E-mail: kajaste.anna@hsr.it

†These authors contributed equally to this work

intracellular loop (CIL), a transmembrane domain (TMD), and a C terminus domain (Bailey *et al.*, 2013; Chesarino *et al.*, 2014b; Ling *et al.*, 2016). IMD and CIL comprise the most evolutionarily conserved domain, known as CD225, in which amino acidic modifications have been associated with altered IFITM3 restriction activity (John *et al.*, 2013; Shi *et al.*, 2021). The identification of several post-translational modifications involved in the regulation of IFITM3 antiviral mechanisms further support this IFITM3 topology (Chesarino *et al.*, 2014b). In mammalian cells, IFITM2 and IFITM3 are mostly present in the early and late endocytic vesicles and on lysosomes (Chesarino *et al.*, 2014a, 2014b; Spence *et al.*, 2019) whereas IFITM1 lacks the endolysosomal sorting motif (YXX Φ) present in both IFITM2 and IFITM3 and is mainly confined at the plasma membrane and early endosomes (Perreira *et al.*, 2013; Bailey *et al.*, 2014).

Severe acute respiratory syndrome coronavirus 2 (SARS-CoV-2) is an enveloped, positive-sense, single-stranded RNA virus, causative agent of COVID-19. Viral entry within the host cell is promoted by the surface spike protein (S) that engages the human receptor ACE2 through its receptor binding domain (RBD). Entry via direct fusion at the plasma membrane or through endocytosis is dictated by the proteolytic cleavage steps imposed by TMPRSS2 or cathepsin L, following ACE2 binding. S protein activation occurs at the plasma membrane when TMPRSS2 is present at the cell surface, whereas endolysosomal S activation occurs when cathepsin L mediates the cleavage (Jackson *et al.*, 2022). Since the first SARS-CoV2 variant was sampled and identified in Wuhan, the emergence of a series of variants, including the most notable lineages B.1.1.7, B.1.351, P1, B.1.617.2, and B.1.529, denominated variants of concern, arise due to different mutations within the spike sequence (Aleem *et al.*, 2022).

Controversial observations regarding the impact of IFITM on SARS-CoV2 have been reported. Human IFITM2 and IFITM3, but not IFITM1, were shown to inhibit SARS-CoV-2 Spike-pseudotyped vesicular stomatitis virus in HEK293T artificially overexpressing ACE2 (Zang *et al.*, 2020). In contrast, all IFITMs, in particular IFITM1, were linked to inhibition of SARS-CoV2 envelope-mediated entry and infection in the same cells (Shi *et al.*, 2021). Moreover, IFITM2, and to some extent IFITM1 but not IFITM3, was observed to block SARS-CoV2 infection in lung epithelial A549 cells overexpressing human ACE2 (Winstone *et al.*, 2021). In addition, endogenous IFITM, in particular IFITM2 and IFITM3, have been suggested to act as entry co-factors for SARS-CoV2 in lung epithelial Calu3 and gut organoids (Prelli Bozzo *et al.*, 2021). Overall, the molecular mechanisms of IFITM-mediated restriction and their role in SARS-CoV2 entry and replication are still debated.

Here, we have investigated the molecular determinants of IFITM-mediated inhibition of plasma membrane versus endosomal viral entry. Our work uncovers distinct mechanisms governing IFITM restriction depending on their cellular localization and identifies a novel IFITM3 interaction interface and cell-type-specific co-factors required for its endosomal antiviral activity.

Results

Cellular localization dictates IFITM restriction preferences

To study IFITM restriction in different cell compartments, we took advantage of pseudotyped lentiviral vectors (LV) to model different

viral entry pathways. IFITM3 has been reported to impede viral egress from the endolysosomal compartments (Perreira *et al.*, 2013). In agreement, LV pseudotyped with VSV-g glycoprotein (VSV-gp) that fuses with the endolysosomal membranes (Cureton *et al.*, 2009) was severely restricted by IFITM3 overexpression in THP1 but was not affected by IFITM1 that predominantly localizes to the plasma membrane (PM; Brass *et al.*, 2009; Bailey *et al.*, 2014; Sun *et al.*, 2020; Fig EV1A–C). In contrast, LV pseudotyped with the measles envelope glycoproteins that mediate fusion directly at the plasma membrane (PM; Plattet *et al.*, 2016) were sensitive to IFITM1 but not affected by IFITM3 (Fig EV1A–C). Noteworthy, plasma membrane confined IFITM3 Y20 phosphomutants that we have previously shown to lose antiviral activity against VSV-gp-pseudotyped LV (Petrillo *et al.*, 2018), inhibited BaEV envelope-, RD114 envelope-, and measles envelope glycoprotein-pseudotyped LV (Fig EV1C) mimicking the antiviral phenotype of IFITM1. Interestingly, also the PM-bound IFITM3- Δ 21 isoform that potentially mimics an IFITM3 variant predicted to be encoded by the human SNP rs-1225-C (Everitt *et al.*, 2012; Compton *et al.*, 2016; Allen *et al.*, 2017) lost antiviral activity against the endosomal entry of VSV glycoprotein but gained restriction against PM-fusing viral entry mediated by the measles glycoproteins (Fig EV1D).

These results indicate that cellular localization of IFITM proteins orients their antiviral activity according to the viral entry route and that our pseudotyped LV transduction assay readily tracks this restriction specificity.

Distinct mechanisms mediate plasma membrane versus endosomal restriction by IFITM3

We took advantage of the pseudotyped LV assay to further dissect IFITM mechanisms of action and made an unexpected observation. IFITM-mediated restriction is proposed to be mainly based on their capacity to alter membrane stiffness or curvature unfavoring viral fusion with cellular membranes (Li *et al.*, 2013; Rahman *et al.*, 2020; Guo *et al.*, 2021). In agreement, Amphotericin B has been shown to abrogate IFITM-mediated restriction of several viruses due to its capacity to bind several lipids including cholesterol and ergosterol altering membrane stability (Lin *et al.*, 2013; Suddala *et al.*, 2019; Rahman *et al.*, 2020). However, Amphotericin B had only a modest impact on IFITM3 restriction of endosomal VSV-gp mediated entry in THP1 cells (Fig 1A) while it fully rescued the antiviral activity of PM-bound mutants of IFITM3 against vectors pseudotyped with the measles virus glycoprotein (Fig 1B). This suggests that distinct mechanisms are involved in plasma membrane versus endosomal IFITM restriction.

To further dissect these mechanistic differences, we leveraged on our observation that the four lysine residues of IFITM3 (Figs 1C and EV1E), conserved across species (Fig 1D), are required for its endosomal antiviral activity against VSV-gp-pseudotyped LV entry (preprint: Unali *et al.*, 2021) to investigate whether these residues would be required also for PM-targeted IFITM restriction. We first confirmed that both the quadruple (4KR) and triple (3KR) lysine to arginine mutants of IFITM3 reduced significantly antiviral activity against endosomal viral entry of VSV-gp-pseudotyped LV (Figs 1E and F, and EV1F). Of note, single lysine mutants did not affect IFITM3 endosomal restriction (Fig EV1G). Interestingly, the three lysine residues within the CIL were not required for antiviral activity

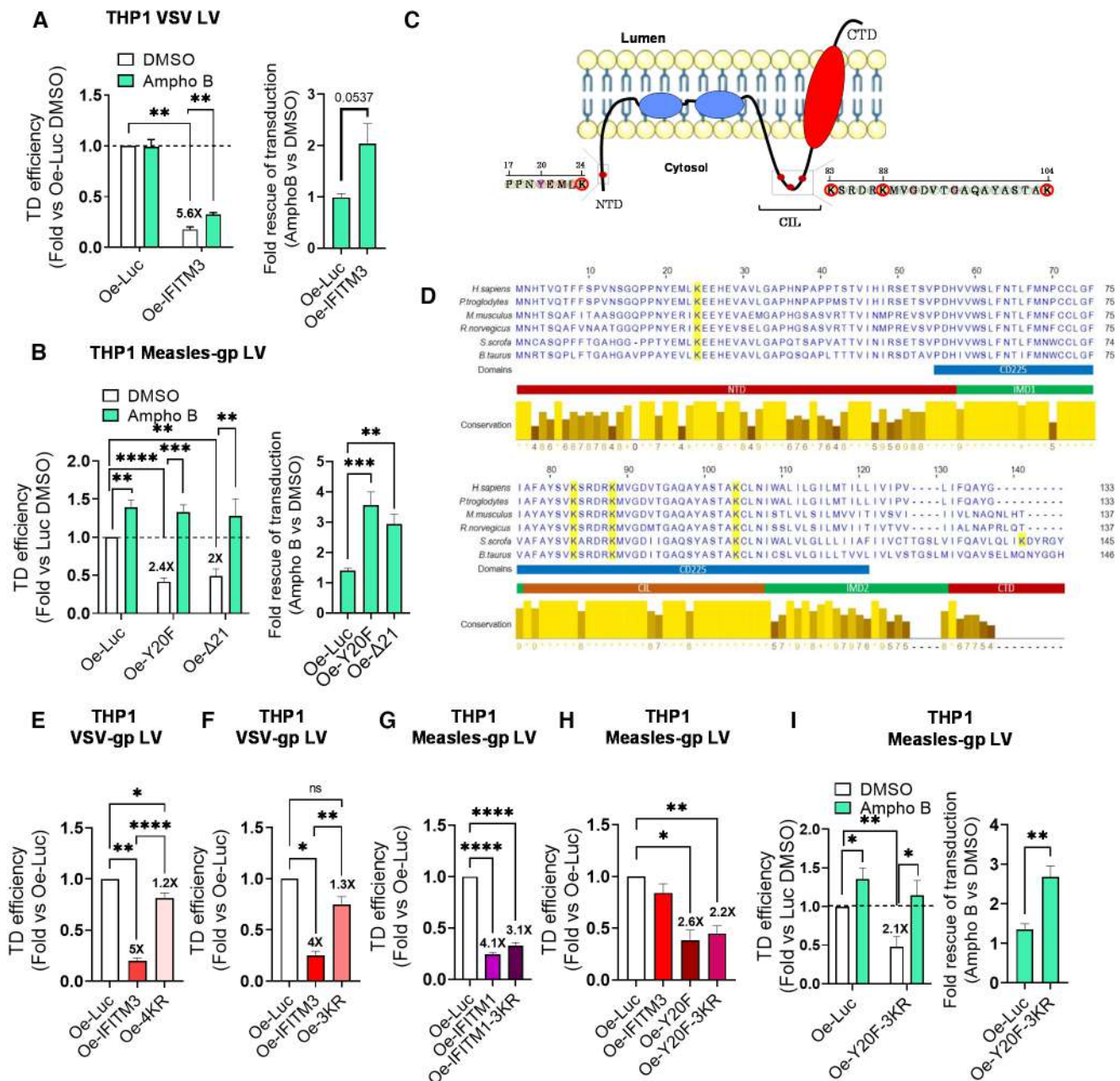


Figure 1. Endosomal and PM-bound IFITM3 restrict viral entry and infection through distinct mechanisms.

- A, B THP1 overexpressing IFITM3, IFITM3-Y20F, IFITM3- Δ 21, or control were pretreated or not with Amphotericin B for 1 h and then transduced with a VSV-gp (A) or measles-gp (B) pseudotyped LV. Transduction efficiencies were evaluated at FACS 5 days later. Fold rescue of transduction over the DMSO control was calculated. Data are shown as mean \pm SEM ($n = 5-8$ biological replicates run in technical duplicate). P -values are for one-sample t -test versus Oe-Luc DMSO = 1, ** for $P < 0.01$, *** for $P < 0.001$.
- C Schematic representation of IFITM3 protein. Lysine residues (K) are highlighted in red.
- D Alignment of IFITM3 orthologs in vertebrates. Conserved lysine residues are marked in yellow.
- E, F THP1 overexpressing IFITM3, IFITM3 lysine-less mutant (4KR) (E), IFITM3 CIL-lysine mutant (3KR) (F), or control were transduced with VSV-gp-pseudotyped LV. Transduction efficiencies were evaluated by flow cytometry 5-day post-TD. Data represent the mean \pm SEM ($n = 9-6$ biological replicates run in technical duplicate). P -values are for one-sample t -test versus Oe-Luc DMSO = 1. * for $P < 0.05$, ** for $P < 0.01$, **** for $P < 0.0001$ and ns for not significant.
- G, H THP1 overexpressing IFITM1, IFITM1-3KR (G), IFITM3, IFITM3-Y20F, IFITM3-Y20F-3KR (H) or control were transduced with measles-gp-pseudotyped LV. Transduction efficiencies were evaluated by flow cytometry 5-day post-TD. Data represent the mean \pm SEM ($n = 4-9$ biological replicates run in technical duplicate). P -values are for one-sample t -test versus Oe-Luc DMSO = 1. * for $P < 0.05$, ** for $P < 0.01$, **** for $P < 0.0001$.
- I THP1 overexpressing IFITM3-Y20F-3KR mutant or control were exposed or not to Amphotericin B for 1 h and then transduced with measles-gp-pseudotyped LV. Transduction levels were measured by flow cytometry 5-day post-TD (mean \pm SEM, $n = 8$ biological replicates run in technical duplicate). P -values are for one-sample t -test versus Oe-Luc DMSO = 1 or Mann-Whitney test for Ampho B versus DMSO in Oe-Y20F-3KR. * for $P < 0.05$, ** for $P < 0.01$.

of IFITM1 against measles-gp-pseudotyped LV (Fig 1G). A similar behavior was observed for the PM-bound IFITM3 mutant Y20F that remained restriction competent and sensitive to Amphotericin B (Figs 1H and I, and EV1H).

Together, these results suggest that different mechanisms of action are involved in plasma membrane versus endosomal restriction by IFITM proteins and identify novel residues within IFITM3 critical for its endosomal antiviral activity.

The lysine residues within the CIL region of IFITM3 mediate interactions with cell-type-specific co-factors required for its endosomal antiviral activity

To investigate why the three lysines within the IFITM3 CIL domain are critical for its endosomal antiviral activity, we first evaluated the impact of the 4KR and 3KR mutations on IFITM3 localization in THP1 as residues within the CD225 domain of IFITM3 have been shown to impact its subcellular trafficking (preprint: Zhong *et al.*, 2021). Differently from the Y20F mutant that confined at the plasma membrane, both lysine mutants colocalized mainly with the LAMP1-positive endosomal compartment similarly to IFITM3-WT (Fig 2A and C). In agreement, only IFITM3-3KR-Y20F mutant but not IFITM3-3KR blocked measles-gp-pseudotyped LV (Fig EV2A). The capacity of IFITM3-3KR to traffic to the lysosome was further confirmed in monocyte-derived macrophages (Fig 2B and C), excluding cellular mislocalization as the cause of lost antiviral activity for the lysine mutant forms of IFITM3. Other amino acid changes in the CD225 domain have been shown to potentially affect IFITM3 dimerization and consequently antiviral activity (John *et al.*, 2013; Zhao *et al.*, 2018b; Rahman *et al.*, 2020). To investigate impact of the 3KR mutation on IFITM3 homodimerization, we set up a proximity ligation assay (PLA) in THP1 cells knockout (KO) for endogenous IFITM3. IFITM3 KO cells were transduced with two lentiviral vectors encoding for HA or His-tagged WT or IFITM3-3KR at limiting doses to achieve a single copy/vector per cell (Fig EV2B and C) and preserved antiviral activity of the tagged IFITM3 proteins was confirmed against VSV-gp-pseudotyped LV (Fig EV2D). PLA foci generated upon proximity of HA and His-tagged proteins were quantified. In contrast to a previously described dimerization mutant (Rahman *et al.*, 2020) that we confirmed to no longer inhibit VSV-gp-pseudotyped LV entry in THP1 (Fig EV2E), no difference in dimerization capacity of WT versus IFITM3-3KR was observed (Fig 2D and E). The capacity of HA/His-IFITM3 and HA/His-3KR to traffic to the endolysosomes was verified by immunofluorescence, and no differences in colocalization were detected (Fig EV2F). In addition, we observed by native electrophoresis that the lysine mutant IFITM3 maintained dimerization capacity as opposed to the dimerization mutant (Figs 2F and EV2G). Together, these results exclude lack of dimerization as the mechanism behind the loss of antiviral activity of the lysine mutant IFITM3.

However, native electrophoresis revealed differences in higher-order protein complex formation with increased ratio of IFITM3 dimers over higher molecular weight complexes for the mutant forms (Fig 2F), suggesting potential loss of co-factor interactions necessary for IFITM3 antiviral activity. In addition, overexpression of IFITM3 (Fig EV2H) was not sufficient to restrict VSV-gp-pseudotyped LV transduction in the myeloid cell line K562 (Fig 3A), indicating the involvement of host factors that are not ubiquitously

expressed across different cell types. Of note, also type I interferon (IFN α) failed to inhibit VSV-gp-pseudotyped LV entry in these cells despite readily inducing expression of IFN-stimulated genes (ISGs), including endogenous IFITM3 (Fig 3B and C). In agreement with a proficient type I IFN response, measles-gp-pseudotyped LV transduction and ZIKA virus infection were significantly hampered in IFN α -stimulated K562, indicating an IFITM3-specific loss of restriction in these cells (Fig 3D and E). Furthermore, despite being incompetent for endosomal IFITM3 restriction, measles-gp LV was readily restricted by both WT and the 3KR lysine mutant IFITM1 (Fig 3F) as well as different PM-bound IFITM3 mutants in K562 in an Amphotericin B-sensitive manner (Fig 3G–I). IFITM3 competence for endolysosomal trafficking was confirmed by IF analysis in K562 (Fig 3J), and Pearson's colocalization coefficients for IFITM3 and LAMP1 were similar in THP1 and K562 (Figs 2C and 3J).

Taken together, our data suggest that the lysine residues within the CIL region of IFITM3 mediate interactions with host factors that are likely absent from K562 cells and required for its antiviral activity within the endosomal compartment but not at the plasma membrane, further supporting the existence of distinct antiviral mechanisms of actions for IFITM depending on their cellular localization.

PIP3 is required for endosomal IFITM3 antiviral activity

To identify host factors required for endosomal IFITM3 antiviral activity, we performed mass spectrometry analysis to define interactomes of WT and 4KR mutant IFITM3 in THP1 cells (Fig EV3A). From a total of 168 proteins pulled down, we identified 74 interactors with higher affinity for lysine-competent IFITM3 (IFITM3-WT), some of which displayed a direct or indirect link with endosomal and lysosomal activities or localization as highlighted in red (Fig 4A and B). Crossing the lysine-competent IFITM3-specific binding proteins with other matching innate immune-related published datasets, we detected an enrichment of proteins interacting with Interferon-stimulated genes (ISG), including IFITM3 (Hubel *et al.*, 2019), with viral immune-modulatory open reading frames (vORFs; Pichlmair *et al.*, 2012), and with the previously described IFITM3-sensitive virus binding proteins (Mairiang *et al.*, 2013; Tripathi *et al.*, 2015; Ammari *et al.*, 2016; Wang *et al.*, 2017; Batra *et al.*, 2018; Coyaud *et al.*, 2018; Gurumayum *et al.*, 2018; Li *et al.*, 2019a; Fig 4C). These results point toward a dynamic interaction between IFITM3 and other potential antiviral protein partners likely explaining the diverse mechanisms of action described so far for this restriction factor.

Among the proteins specifically binding to the lysine-competent form of IFITM3, we identified proteins involved in viral entry and transport, regulation of viral life cycle, endosomal transport, toll-like receptor and intracellular signaling pathways (Fig 4D). In agreement with the absence of lysine residues, the 4KR IFITM3 mutant failed to interact with proteins implicated in ubiquitin ligase binding and K63-linked ubiquitination, key modifications required for the regulation of innate immunity (Madiraju *et al.*, 2022; Fig 4B and E). Moreover, we identified interactions with phosphatidylinositol binding proteins that were specific for the lysine-competent IFITM3-WT (Fig 4E).

This interaction of the lysine-competent IFITM3 with several phosphatidylinositol binding proteins caught our attention as

phosphatidylinositol is directly linked to the regulation of innate immune signal transduction in several contexts (Barnett & Kagan, 2020). We performed proximity ligation assays to investigate IFITM3 interaction with Phosphatidylinositol 3,4,5-trisphosphate (PIP3) in our experimental setting and probed the role of the CIL

domain lysines in it. Interestingly, the 3KR-IFITM3 mutant interacted significantly less with PIP3 compared with IFITM3-WT (Figs 5A and EV3B) supporting a role of these residues in IFITM3 interaction with PIP3. Immunofluorescence analysis showed similar colocalization of the tagged IFITM3-3KR, PIP3, and LAMP1 in

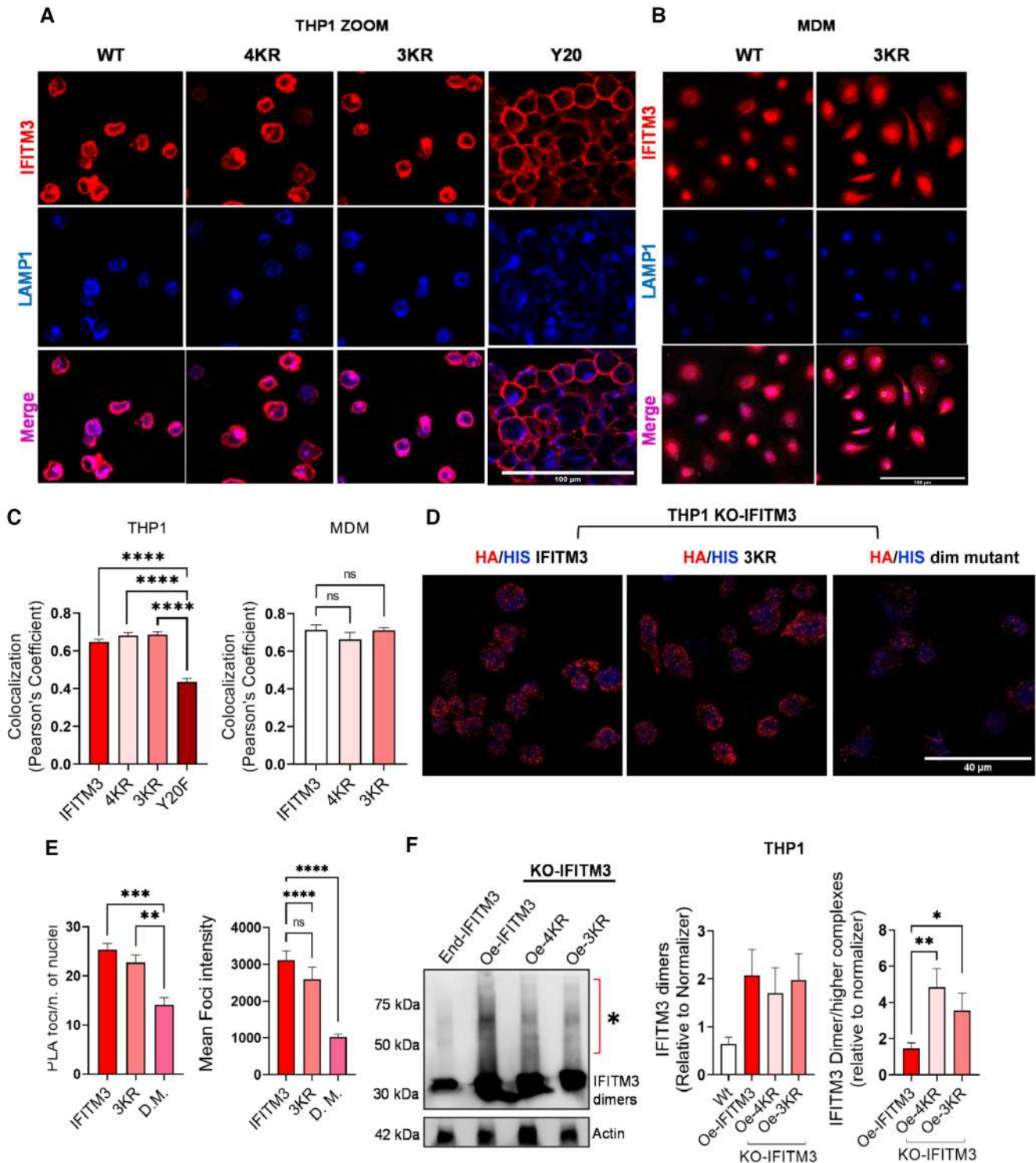


Figure 2.

Figure 2. Conserved lysine residues and cell-type-specific co-factors are required for endosomal IFITM3 restriction.

- A, B Immunofluorescence images were performed using TCS SP5 Leica confocal microscope, 60 \times with oil on THP1 overexpressing IFITM3-WT, IFITM3-4KR, IFITM3-3KR, or IFITM3-Y20F (A) ($n = 22$ images acquired from three biological replicates) and primary monocyte-derived macrophages (MDM) overexpressing IFITM3-WT, IFITM3-4KR, IFITM3-3KR (B) ($n = 12$ images acquired from three independent donors). Colocalization (purple areas) of IFITM3 (in red) with the lysosome-associated membrane protein 1 (LAMP1) marker (in blue) was evaluated. Representative zoomed images are shown, scale bar 100 μ m.
- C Quantification of Pearson's colocalization coefficient was performed on Oe-THP1 and MDM ($n = 22$ –12 images acquired from three biological replicates).
- D IFITM3-IFITM3 interactions (red dots) were evaluated by proximity ligation assay (PLA) in THP1 knockout for endogenous IFITM3 and expressing either HA-IFITM3 and His-IFITM3, HA-3KR and His-3KR or His-dimer mutant IFITM3 (D.M) and HA-dimer mutant. Images were acquired on TCS SP5 Leica confocal microscope 60 \times with oil. Representative images are shown ($n = 8$ images of four biological replicates), scale bar 40 μ m.
- E Number of foci and PLA foci intensity were measured on ImageJ and normalized over the number of nuclei (mean \pm SEM, $n = 4$ biological replicates).
- F IFITM3 dimerization was assessed by native PAGE followed by WB analysis in THP1. IFITM3 higher-order protein complex bands are highlighted by the asterisk. IFITM3 dimers and higher molecular weight complexes were quantified over the normalizer using ImageJ (mean \pm SEM, $n = 7$ biological replicates). P -values are for Mann-Whitney test. * for $P < 0.05$, ** for $P < 0.01$.

Source data are available online for this figure.

comparison with the tagged IFITM3-WTs further, indicating that loss of interaction with PIP3 is not determined by altered IFITM3-3KR localization (Fig EV3C). In addition, quantification of PIP3 in both 3KR-IFITM3 mutant and IFITM3-WT overexpressing THP1 was performed to exclude differences of PIP3 levels in the two cell lines (Figs 5B and EV3D).

Among the different downstream effectors of PIP3 signaling, we focused on mTOR as mTOR inhibitors were previously reported to counteract IFITM3 antiviral activity against Influenza A and VSV-gp-pseudotyped LV in HeLa cells and human hematopoietic stem cells (HSC; Shi *et al*, 2018; Ozog *et al*, 2019). We confirmed that mTOR inhibition counteracts IFITM3-mediated restriction of VSV-gp-pseudotyped LV entry also in THP1 overexpressing IFITM3 (Fig 5C). The beneficial effect of Rapamycin on VSV-gp-pseudotyped LV transduction was IFITM3-dependent as IFN α -induced IFITM3 antiviral activity and Rapamycin-mediated rescue of transduction were lost in THP1 knockout for IFITM3 (Fig EV3E). Of note, Rapamycin did not improve transduction of measles-gp-pseudotyped LV in THP1 overexpressing the PM-bound IFITM3-3KR mutant (Fig 5D), suggesting it acts specifically at the level of endosomal restriction. In agreement, Rapamycin enhanced VSV-gp-pseudotyped LV transduction in human hematopoietic cells (HSC; Petrillo *et al*, 2015) that express high basal levels of IFITM3 (Petrillo *et al*, 2018) but did not improve measles-gp-pseudotyped LV transduction in these cells (Fig 5E).

Binding with PIP3 has been described to cause phosphorylation and subsequent activation of Akt (Czech, 2000; Denley *et al*, 2009; Gan *et al*, 2011; Liu *et al*, 2015). To probe the role of Akt in PIP3-mediated IFITM3 endosomal antiviral activity, we tested the Akt inhibitor MK2206 in THP1 overexpressing cells and HSC. Like Rapamycin, MK2206 counteracted IFITM3-mediated inhibition of VSV-gp-pseudotyped LV transduction in THP1 and HSC (Fig 5F and G). Phosphoinositide 3-kinase (PI3K) acts upstream of the Akt–mTOR pathway and is responsible for PIP2 conversion into PIP3 (Vanhaesebroeck *et al*, 2010). To investigate the involvement of PI3K in IFITM3 endosomal restriction, we treated THP1 overexpressing IFITM3, KO-IFITM3 or controls with the PI3K inhibitor LY294002 for 24 h. In line with a lower synthesis of PIP3 upon PI3K blockage, LY294002 partly alleviated IFITM3 restriction on VSV-gp-pseudotyped LV (Fig 5H). A modest although not significant effect was observed also in the Oe-Luc control that expresses IFITM3 endogenously but not in IFITM3 KO THP1 in which endogenous IFITM3 was depleted. These results indicate that the potency of

IFITM3 antiviral activity may correlate with PIP3 levels and point toward a mechanism of action that is PI3K-Akt–mTOR dependent as depicted in the model in Fig 5I.

Together, these data identify host factors specifically interacting with the endosomal restriction-competent IFITM3 and define PIP3 as a critical host factor required for endosomal IFITM3 restriction linking it to the PI3K/Akt/mTOR pathway.

Low cellular PIP3 content tracks with impaired endosomal IFITM3 restriction

Given our observation regarding the key role of PIP3 in IFITM3 restriction, we investigated whether altered phospholipid metabolism could explain the lack of IFITM3 antiviral activity in K562 cells. To this end, we performed transcriptomic and lipidomic analysis comparing the IFITM3 restriction-competent THP1 and HSPC to K562. Comparative transcriptomics revealed that phosphatidylinositol's binding together with antiviral responses, including defense to virus and regulation of viral entry and release from the host, were among the top enriched pathways in HSPC and THP1 in comparison with K562 (Fig 6A). In agreement, lower levels of PI3K genes and genes involved in phosphatidylinositol phosphate binding were detected in K562 in comparison with THP1 and HSPC (Fig 6B). In addition, lipidomic profiling revealed that K562 cells have significantly lower basal levels of different phosphatidylinositol (PI) species (Fig EV4A), including PIP3 precursors, when compared to THP1 and HSPC (Fig 6C and D). Immunofluorescence analysis confirmed that K562 overexpressing IFITM3 harbor significantly reduced amounts of PIP3 than THP1 overexpressing IFITM3 (Figs 6E and EV4B). Consistent with their lower PIP3 content, a significantly lower number of PLA foci between PIP3 and IFITM3 as well as a reduced PLA foci intensity were detected in K562 cells compared with THP1 as measured by proximity ligation assays (Fig 6F).

Interestingly, while IFN α induced both IFITM3 and PIP3 levels in restriction-competent THP1 cells, only IFITM3 levels increased in K562 (Figs 6G and EV4C). These data suggest that sufficient levels of both IFITM3 and PIP3 are required to achieve efficient endosomal antiviral restriction. In agreement, primary CD34⁺ HSPC that are highly refractory to endosomal viral entry (Petrillo *et al*, 2018) harbor high endogenous levels of both IFITM3 and PIP3 (Figs 6H and EV4D) that can be achieved by IFN α stimulation in other primary human blood cells such as monocyte-derived macrophages (Figs 6I

and EV4E). Importantly, endosomal IFITM3 restriction against VSV-gp-pseudotyped LV was restored by providing exogenous PIP3 to K562 (Figs 6J and EV4F). This rescue was lower in cells knockout for IFITM3 (Fig 6J) and specific for endosomal restriction as PIP3 addition did not affect entry of the PM-fusing measles-gp-pseudotyped LV (Fig EV4G). Noteworthy, exogenous delivery of PIP3 significantly potentiated endosomal antiviral activity also in HSPC further suggesting a positive correlation between PIP3 content and viral inhibition (Fig 6K).

Overall, our data indicate that sufficient PIP3 and IFITM3 levels are required for effective endosomal restriction that can be restored

and potentiated by modulating levels of intracellular PIP3, rendering it an attractive target to boost antiviral immunity against viral pathogens that enter through endocytosis.

Lysine-dependent PIP3 scaffolding is required for IFITM endosomal restriction and can be harnessed to potentiate viral inhibition

To test this hypothesis, we investigated the novel mechanisms of plasma membrane versus endosomal restriction of IFITM proteins against replicating viral pathogens, including SARS-CoV2. As SARS-

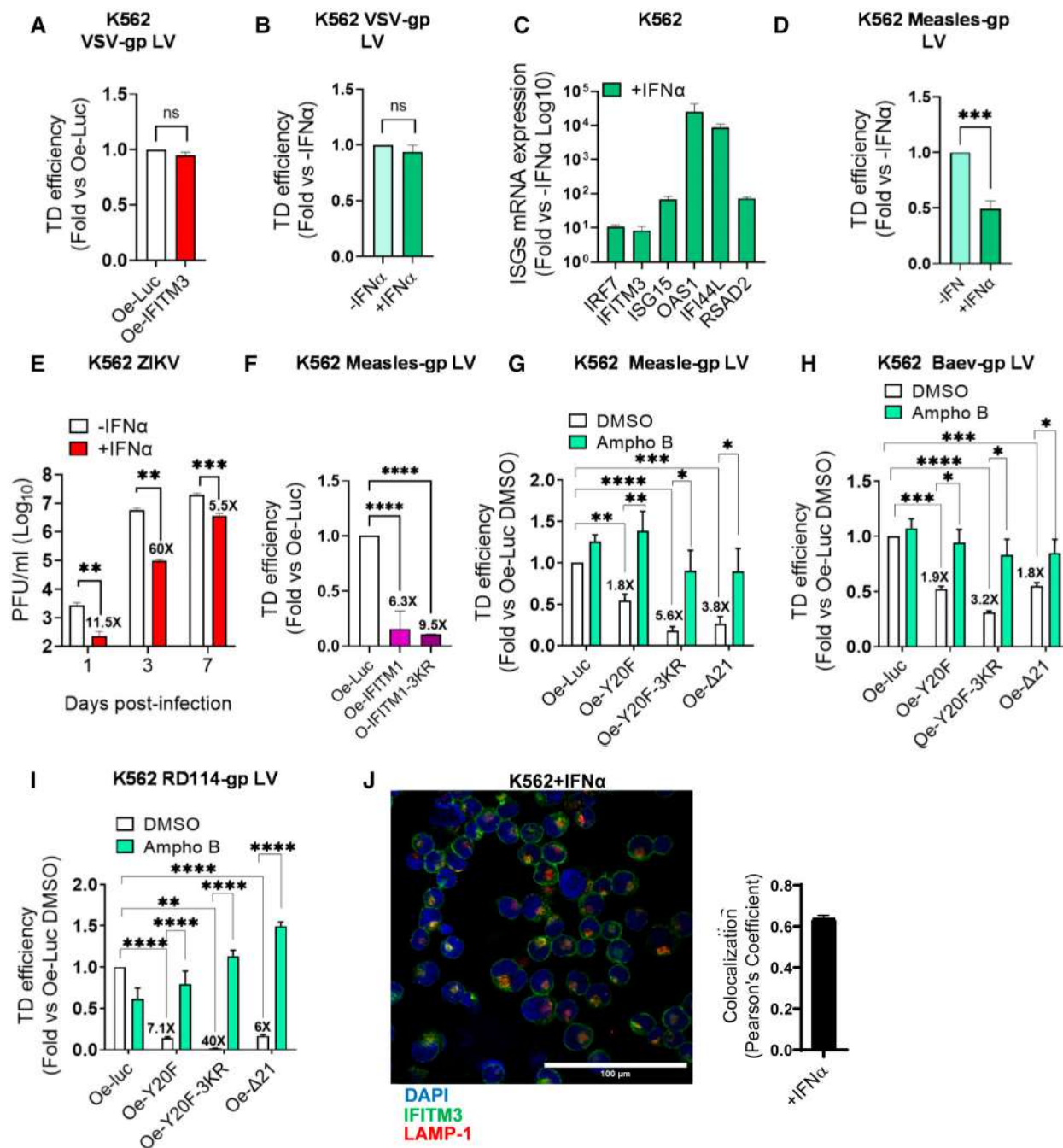


Figure 3.

Figure 3. K562 respond to type I IFN but are insensitive to IFITM3 restriction.

- A K562 overexpressing IFITM3 or control were transduced with VSV-gp-pseudotyped LV (mean \pm SEM, $n = 6$ biological replicates run in technical duplicate). Transduction levels were calculated at FACS 5-day post-TD measuring the % of BFP expression within Oe-cells. Data are represented as Folds over the Oe-Luc control. P -values are for one-sample t -test versus Oe-Luc = 1. ns for not significant.
- B K562 were prestimulated with IFN α and then transduced with VSV-gp-pseudotyped LV. Transduction was evaluated 5 days after TD (mean \pm SEM, $n = 4$ biological replicates run in technical duplicate). Data are represented as Folds over the Oe-Luc control. P -values are for one-sample t -test versus -IFN α = 1. ns for not significant.
- C Interferon-stimulated genes (ISGs) mRNA expression were measured 24-h post-IFN α stimulation by RT-qPCR in K562 (mean \pm SEM, $n = 3$ biological replicates run in technical duplicate).
- D K562 were prestimulated with IFN α and then transduced with measles-gp-pseudotyped LV. Transduction was measured 5-day post-TD (mean \pm SEM, $n = 3$ biological replicates run in technical duplicate). P -values are for one-sample t -test versus -IFN α = 1. *** for $P < 0.001$.
- E K562 were prestimulated or not with IFN α for 24 h and then inoculated with the infectious ZIKV (mean \pm SEM, $n = 3$ biological replicates run in technical triplicates). Viral supernatant was collected at different time points and titered on Vero E6 cells. P -values are for Mann-Whitney test. ** for $P < 0.01$, *** for $P < 0.001$.
- F K562 overexpressing IFITM1, IFITM1-3KR, or control were transduced with measles-gp-pseudotyped LV. Transduction efficiency was evaluated 5-day post-TD (mean \pm SEM, $n = 4$ biological replicates run in technical duplicate). P -values are for one-sample t -test versus Oe-Luc = 1. **** for $P < 0.0001$.
- G-I K562 overexpressing IFITM3, IFITM3-Y20F, IFITM3-Y20F-3KR, or control were pre-exposed or not to Ampho B and then transduced with measles-gp (G), BaEV-gp (H) or RD114-gp (I) pseudotyped LV. Transduction efficiencies were measured by flow cytometry 5 days after TD (mean \pm SEM, $n = 5$ –4–4 biological replicates run in technical duplicate). P -values are for one-sample t -test versus Oe-Luc DMSO = 1 or unpaired t -test for Ampho B versus DMSO. * for $P < 0.05$, ** for $P < 0.01$, *** for $P < 0.001$, **** for $P < 0.0001$.
- J IFITM3 localization was analyzed by IF in K562, a representative zoomed image is shown ($n = 12$ images of three biological replicates), scale bar 100 μ m. Pearson's colocalization coefficient was measured with ImageJ.

CoV2 has been described to utilize both plasma membrane and endosomal entry routes depending on the expression of entry co-factors such as TMPRSS2 (Jackson *et al*, 2022), we first investigated to the role of IFITM in restricting its entry into relevant target cells. To this end, we tested the impact of IFITM on entry mediated by the SARS-CoV2 Spike protein isolated from the original Wuhan strain in human lung epithelial Calu3 cells using the pseudotyped LV entry assay or a replicating Wuhan SARS-CoV2 isolate (Figs 7A and B, and EV5A). Only overexpression of IFITM1 led to a significant reduction of SARS-CoV2 entry and viral replication in Calu3, while IFITM2 and IFITM3 overexpression slightly promoted it (Fig 7A and B), suggesting that this Spike variant enters mainly via the plasma membrane. Interestingly, also the PM-confined IFITM3 phosphomutant Y20A gained antiviral activity against SARS-CoV2 Spike-gp-pseudotyped vectors (Fig 7A) and replicating virus (Figs 7C and EV5A) that was also restricted by the PM-bound putative IFITM3- Δ 21 isoform that has been predicted to potentially mimic an IFITM3 variant to be encoded by the human SNP rs-1225-C (Everitt *et al*, 2012; Compton *et al*, 2016; Allen *et al*, 2017; Figs 7D and EV5B), further supporting a PM-dependent entry mechanism for SARS-CoV2 Wuhan variant in Calu3 cells. This pattern of restriction was confirmed across Spike proteins belonging to pre-Omicron variants of concern (Fig EV5C), and similar results were obtained also in the pro-monocytic THP1 cells (Figs 7E and F, and EV5D) that we found to express unusually high levels of ACE2 and TMPRSS2 (Fig EV5E–G) and efficiently support SARS-CoV2 replication (Fig 7E). In agreement with a recently proposed endosomal entry mechanism for the recent SARS-CoV2 Omicron variant (Pia & Rowland-Jones, 2022; Zhao *et al*, 2022), Omicron Spike-gp-pseudotyped LV were susceptible to both IFITM1 and IFITM3 in Calu3 cells (Fig 7G), and replicating SARS-CoV2 Omicron was mostly restricted by the endosomal IFITM2 and IFITM3 but remained susceptible also to IFITM1 and the PM-bound IFITM3 mutant (Fig 7H and I).

Of note, in cellular systems overexpressing the SARS-CoV2 receptor ACE2 (Scialo *et al*, 2020) such as the lung epithelial cell line A549 (Fig EV5H and I) or nonhuman cell lines such as the African

Green monkey kidney Vero cells (Fig EV5J), all three antiviral IFITM reduced SARS-CoV2 replication with IFITM1 remaining the strongest inhibitor (Fig EV5K and L), indicating that careful selection of physiological systems and human cell lines are required to study antiviral defenses against SARS-CoV2 entry.

In agreement with a role in endosomal antiviral immunity, the three lysine residues within the IFITM3 CIL were necessary against endocytosis-dependent viruses such as VSV and ZIKV (Fig 8A and B) and requirement for cell-type-specific factors was confirmed as FITM3-WT failed to restrict these endocytic viruses in K562 cells (Fig 8C and D). Conversely, these lysines were not required for IFITM3 antiviral activity at the plasma membrane as the PM-bound IFITM3 mutant Y20F maintained restriction against infectious Wuhan SARS-CoV2 isolate in THP1 and Calu3 even when these lysines were mutated (Figs 8E and F, and EV5M). Interestingly instead, endosomal IFITM3 restriction against replicating SARS-CoV2 Omicron was completely abrogated when the lysines of the CIL domain were mutated while all PM-confined IFITM3 mutants maintained antiviral activity regardless of the presence or not of these lysines (Fig 8G), further highlighting that the CIL domain lysine residues are required exclusively for IFITM3 endosomal antiviral activity.

Finally, and in line with the hypothesis that low cellular PIP3 levels impair endosomal IFITM3 restriction in K562, exogenous PIP3 delivery restored IFITM3 antiviral activity against infectious VSV in these cells (Fig 8H). Importantly, addition of PIP3 significantly boosted IFITM3 restriction against the Omicron SARS-CoV2 variant of concern (Fig 8I). This effect was IFITM3-dependent as PIP3 delivery did not block infection in K562 or Calu3 cells KO for IFITM3 (Fig 8H and I). In addition, both IFITM3 and PIP3 levels were significantly upregulated upon Omicron infection in Calu3 cells (Fig 8J), further supporting a coordinated antiviral role of IFITM3 and PIP3.

Together, these data indicate that manipulating cellular PIP3 levels can be exploited to potentiate IFITM3 restriction against endocytosis-dependent viruses including Omicron and potentially other novel emerging SARS-CoV2 variants of concern.

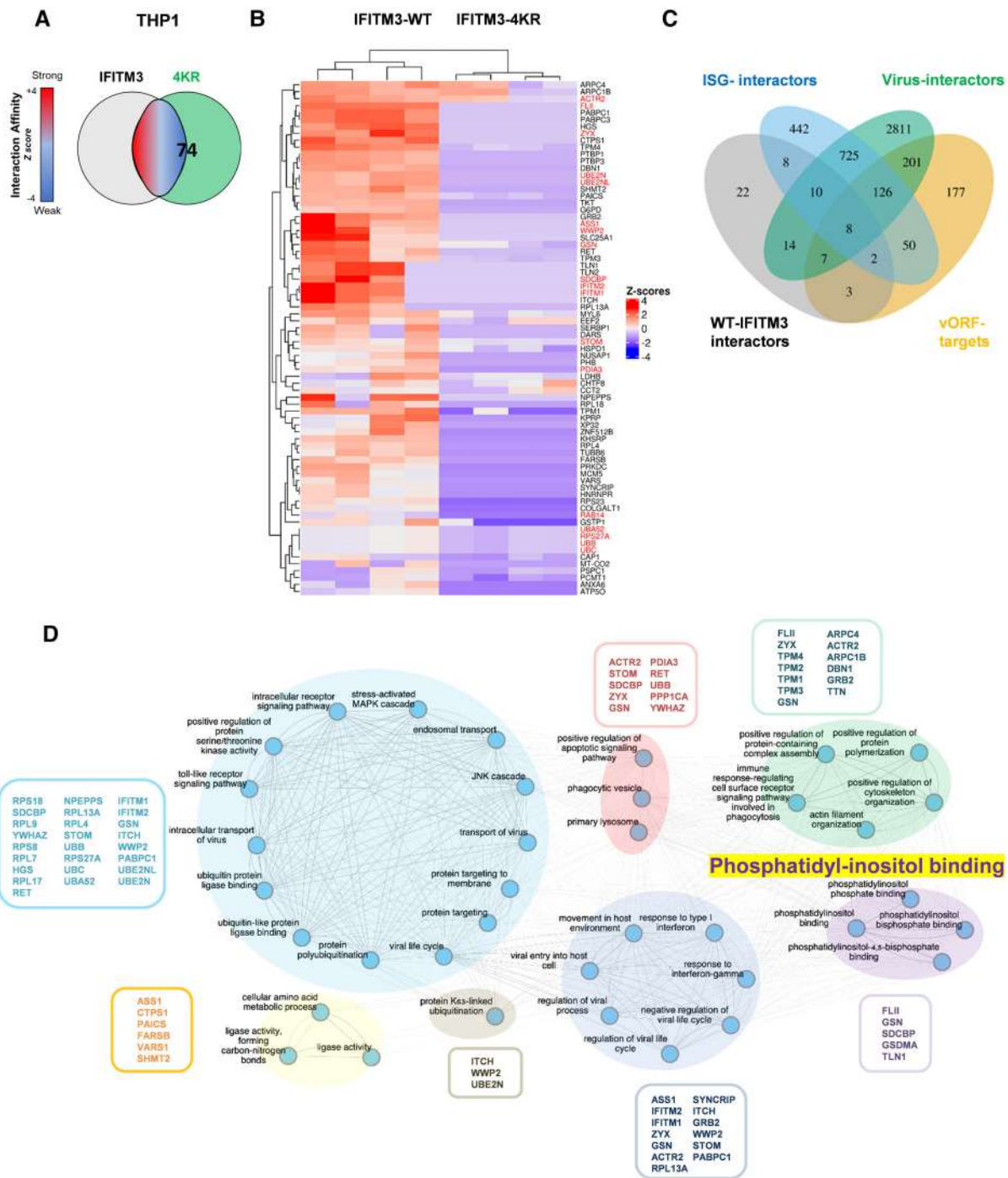


Figure 4. Analysis of lysine-competent IFITM3 interactions.

- A Venn diagram of wild-type (WT) IFITM3 (gray marking) and 4KR-IFITM3 (green marking) interactors identified by mass spectrometry in THP1.
- B IFITM3-WT or IFITM3-4KR were immunoprecipitated in THP1, interactors were identified by mass spectrometry. The heatmap shows proteins with significant higher affinity for IFITM3-WT compared with IFITM3-4KR (Benjamini–Hochberg FDR < 0.05). In red interactors linked or localizing in endosomes and lysosomes.
- C Venn diagram of IFITM3 interactors (gray marking, 74 proteins) ISG interactors (turquoise marking, 1,371 proteins), vORF interactors (yellow marking, 574 proteins), and viral interactors (green marking, 3,902 proteins). The labels indicate the number of proteins in the overlaps of the dataset.
- D IFITM3 interactors protein map and functionally enriched terms (Benjamini–Hochberg FDR < 0.05). Phosphatidylinositol binding is highlighted in yellow.

Discussion

Our work sheds light on molecular mechanisms of IFITM-mediated restriction of viral entry revealing cell-compartment-specific mechanisms of action and uncovering the requirement of co-factors for endosomal antiviral immunity. Among the antiviral IFITM, IFITM3 has been the best characterized for blocking a broad range of viruses (Brass *et al*, 2009; Lu *et al*, 2011; Perreira *et al*, 2013; Bailey *et al*, 2014; Zhao *et al*, 2018a; Zang *et al*, 2020; Shi *et al*, 2021).

However, a detailed molecular mechanism of action has not been identified yet. Our work uncovers an unexpected mechanistic difference between endosomal and plasma membrane IFITM restriction. IFITM3 restriction has been linked to its capacity to increase membrane stiffness and impede fusion between viral and host membranes (Li *et al*, 2013; Rahman *et al*, 2020; Guo *et al*, 2021). In agreement, Amphotericin B has been shown to prevent IFITM3-mediated inhibition of IAV through modulating membrane fluidity (Lin *et al*, 2013; Suddala *et al*, 2019; Rahman *et al*, 2020). However,

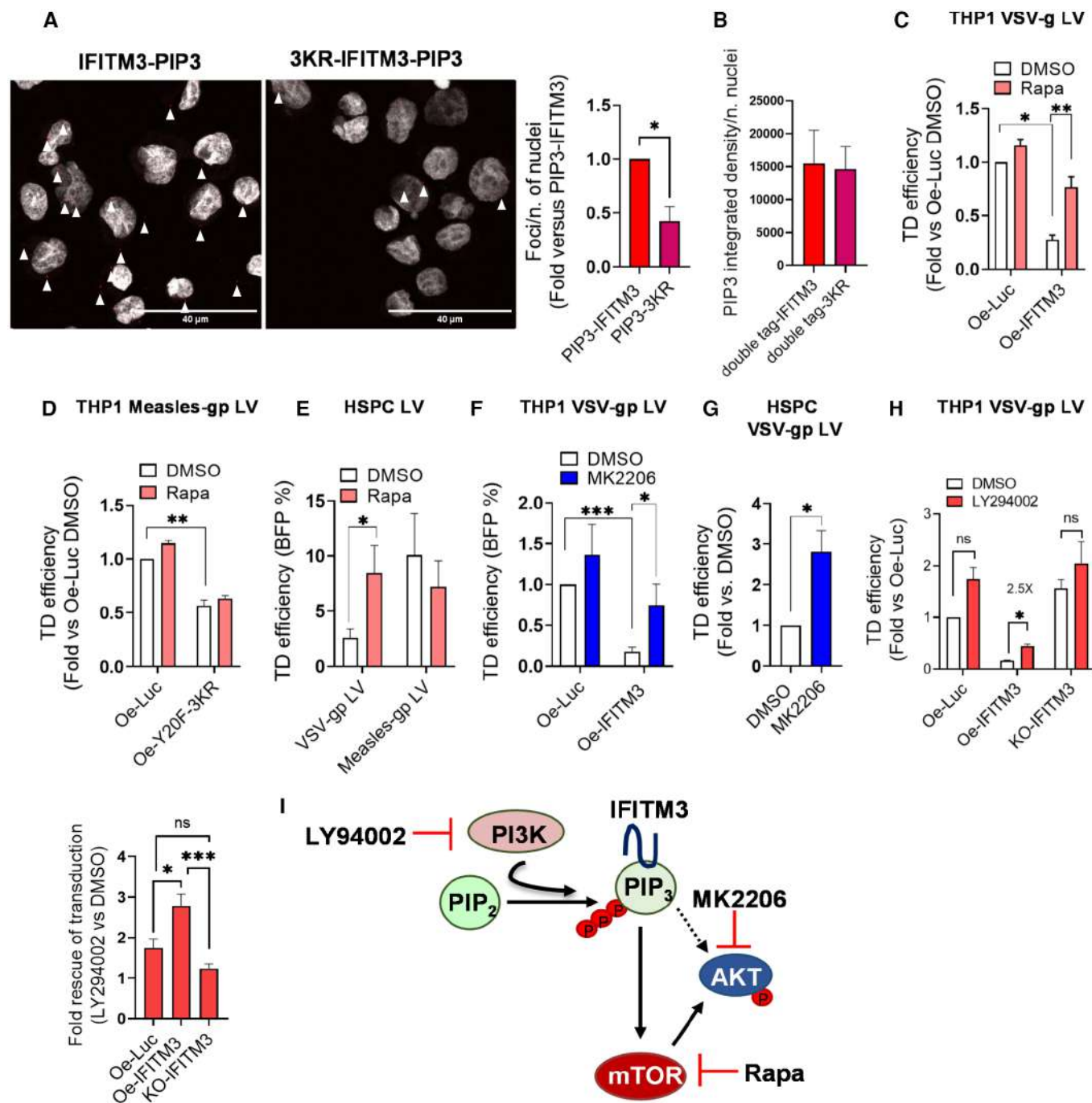


Figure 5.

Figure 5. PIP3 interaction and signaling cascade through the PI3K-mTOR-AKT axes are required for endosomal IFITM3 antiviral activity.

- A Interaction between IFITM3 wild-type or 3KR and Phosphatidylinositol-3 phosphate (PIP3; red dots) was evaluated by proximity ligation assay. Images were acquired using TCS SP5 Leica confocal microscope 60× with oil in THP1 knockout for endogenous IFITM3 and expressing either IFITM3 wild-type or IFITM3-3KR. Number of foci were counted on ImageJ and normalized over the number of nuclei (mean ± SEM, $n = 5$ biological replicates). White arrows indicate foci, scale bar 40 μm.
- B Phosphatidylinositol-3 phosphate (PIP3) levels were measured by immunofluorescence in THP1 overexpressing the His-IFITM3/HA-IFITM3 and His-3KR/HA-3KR. PIP3 was quantified via ImageJ (mean ± SEM, $n = 5$ biological replicates).
- C THP1 overexpressing IFITM3 or control were transduced with VSV-gp-pseudotyped LV in the presence or absence of Rapamycin (Rapa). Transduction efficiency was measured at FACS 5-day post-TD (mean ± SEM, $n = 6$ biological replicates run in technical duplicate). P -values are for one-sample t -test versus Oe-Luc DMSO = 1 and Mann-Whitney test for Rapa versus DMSO. ** for $P < 0.01$, **** for $P < 0.0001$.
- D THP1 overexpressing IFITM3-Y20F-3KR or control were exposed or not to Rapamycin and transduced with measles-gp-pseudotyped LV. Transduction efficiency was evaluated by flow cytometry 5-day post-TD (mean ± SEM, $n = 4$ biological replicates run in technical duplicate). P -values are for one-sample t -test versus Oe-Luc DMSO = 1. ** for $P < 0.01$.
- E Hematopoietic stem and progenitor cells (HSPC) were transduced with VSV-gp or measles-gp-pseudotyped LV in the presence or absence of Rapamycin. Transduction was evaluated at FACS 5 days later measuring the % of BFP expression (mean ± SEM, $n = 4$ biological replicates run in technical duplicate). P -values are for Mann-Whitney test. * for $P < 0.05$.
- F THP1 overexpressing IFITM3 or control were transduced with VSV-gp-pseudotyped LV in the presence or absence of MK2206. Transduction efficiency was analyzed 5-day post-TD (mean ± SEM, $n = 6$ biological replicates run in technical duplicate). P -values are for one-sample t -test versus Oe-Luc DMSO = 1 and for Mann-Whitney test for Oe-IFITM3 DMSO versus MK2206, * for $P < 0.05$, *** for $P < 0.001$.
- G Human hematopoietic stem and progenitor cells were pretreated with MK6602 for 1 h and then transduced with VSV-gp-pseudotyped LV (mean ± SEM, $n = 4$ biological replicates run in technical duplicate). P -values are for one-sample t -test versus Oe-Luc DMSO = 1. * for $P < 0.05$.
- H THP1 overexpressing IFITM3, KO-IFITM3, or control were transduced with VSV-gp-pseudotyped LV after 4 h of pretreatment with LY94002. Transduction efficiency was analyzed 5-day post-TD (mean ± SEM, $n = 5$ biological replicates run in technical duplicate). P -values are for one-sample t -test versus Oe-Luc DMSO and Mann-Whitney test for IFITM3 DMSO versus IFITM3 LY294002, KO-IFITM3 DMSO versus KO-IFITM3 LY294002 as well as for fold rescue of transduction. * for $P < 0.05$, *** for $P < 0.001$.
- I Schematic representation of IFITM3-PIP3 signaling cascade acting on the PI3K-mTOR-AKT axes, respectively, blocked by Rapamycin and MK2206.

IFITM3 restriction of VSV-gp-pseudotyped LV could not be rescued by Amphotericin B, suggesting that the mechanism of action does not rely on membrane stability in this context. Instead, Amphotericin B rescued inhibition of PM-fusing vectors by IFITM3-PM mutants, indicating that the mechanisms involved in IFITM restriction of PM and endocytosis-dependent viral entry are distinct. In agreement, the lysine residues within the CIL domain of IFITM3 were required only for its endosomal antiviral activity but dispensable for restriction of PM-fusing viruses. A similar lysine-less mutant IFITM3 has been shown to better control Influenza infection due to the loss of its ubiquitin-mediated degradation (Yount *et al*, 2012; Shi *et al*, 2018). It is possible that the neutral alanine residues used in these studies in substitution of lysines differently affect IFITM3

conformation compared with the positively charged arginine residues used here. Interestingly, two lysine residues within the intracellular loop of IFITM1 were also described as important for its antiviral activity against Flaviviruses (Sun *et al*, 2020), suggesting they play a key antiviral role across all antiviral IFITM. However, these lysines were not necessary for IFITM1 antiviral activity against PM-fusing LV further underscoring the cell-compartment specificity of IFITM antiviral mechanisms.

Mutations of the lysine residues of IFITM3 protein have not been linked to altered protein conformation (Ling *et al*, 2016), but other amino acidic modifications within the CIL domain were associated with dimerization defects (John *et al*, 2013; Rahman *et al*, 2020) and absence of antiviral activity. Our data indicate that the IFITM3

Figure 6. PIP3 is an interferon-regulated phospholipid required for IFITM3 antiviral activity.

- A RNA sequencing performed in HSPC (CD34), THP1, and K562. Pathways differentially regulated in HSPC and THP1 in comparison with K562 are highlighted.
- B Heatmap representation of genes involved in PI3K and phosphatidylinositol phosphate binding pathway. Upregulated genes are shown in red, and downregulated genes are shown in blue.
- C, D Levels of phosphatidylinositol (PI) precursors of PIP3 and PIP2 were measured through lipidomic analysis in THP1, HSPC, and K562. The results are presented as log plots of the PI ratio in K562 over THP1 (C) or HSPC (D).
- E PIP3 levels were measured by immunofluorescence (scale bar 40 μm) and quantified as integrated density with ImageJ software in THP1 and K562 overexpressing IFITM3 (mean ± SEM, $n = 3$ biological replicates). P -values are for Mann-Whitney test, * for $P < 0.05$.
- F Interaction between IFITM3 and Phosphatidylinositol-3 phosphate (PIP3; red dots) was evaluated by proximity ligation assay using TCS SP5 Leica confocal microscope 60× with oil in THP1 or K562 expressing same levels of IFITM3. Number of foci and PLA foci intensity were measured on ImageJ and normalized over the number of nuclei (mean ± SEM, $n = 4$ biological replicates run in technical duplicate), scale bar 40 μm. P -values are for Mann-Whitney test, ** for $P < 0.01$, *** for $P < 0.001$.
- G-I PIP3 levels were measured by immunofluorescence and quantified as integrated density with ImageJ software in THP1 and K562 (G), HSPC (H), and MDM (I) prestimulated or not with IFNα (mean ± SEM, $n = 3$ biological replicates). P -values are for Mann-Whitney test, *** for $P < 0.001$.
- J PIP3 coupled to a specific PIP carrier (PIP3 + Carr Ctrl) or Carr Ctrl alone were delivered to K562 overexpressing IFITM3, control or KO for IFITM3. All conditions were transduced with VSV-gp-pseudotyped LV. Transduction levels were evaluated 5-day post-TD (mean ± SEM, $n = 5$ biological replicates run in technical duplicate). P -values are for one-sample t -test versus Ctrl Carr = 1. * for $P < 0.05$, ** for $P < 0.01$. The effect on transduction of exogenous PIP3 in K562 is represented as Fold versus Carr Ctrl.
- K HSPC pretreated with PIP3 coupled to a specific PIP carrier (PIP3 + Carr Ctrl) or Carr Ctrl alone were transduced with VSV-gp-pseudotyped LV. Transduction levels were evaluated 5-day post-TD measuring the % of BFP expression (mean ± SEM, $n = 5$ biological replicates run in technical duplicate). P -values are for Mann-Whitney test, * for $P < 0.05$.

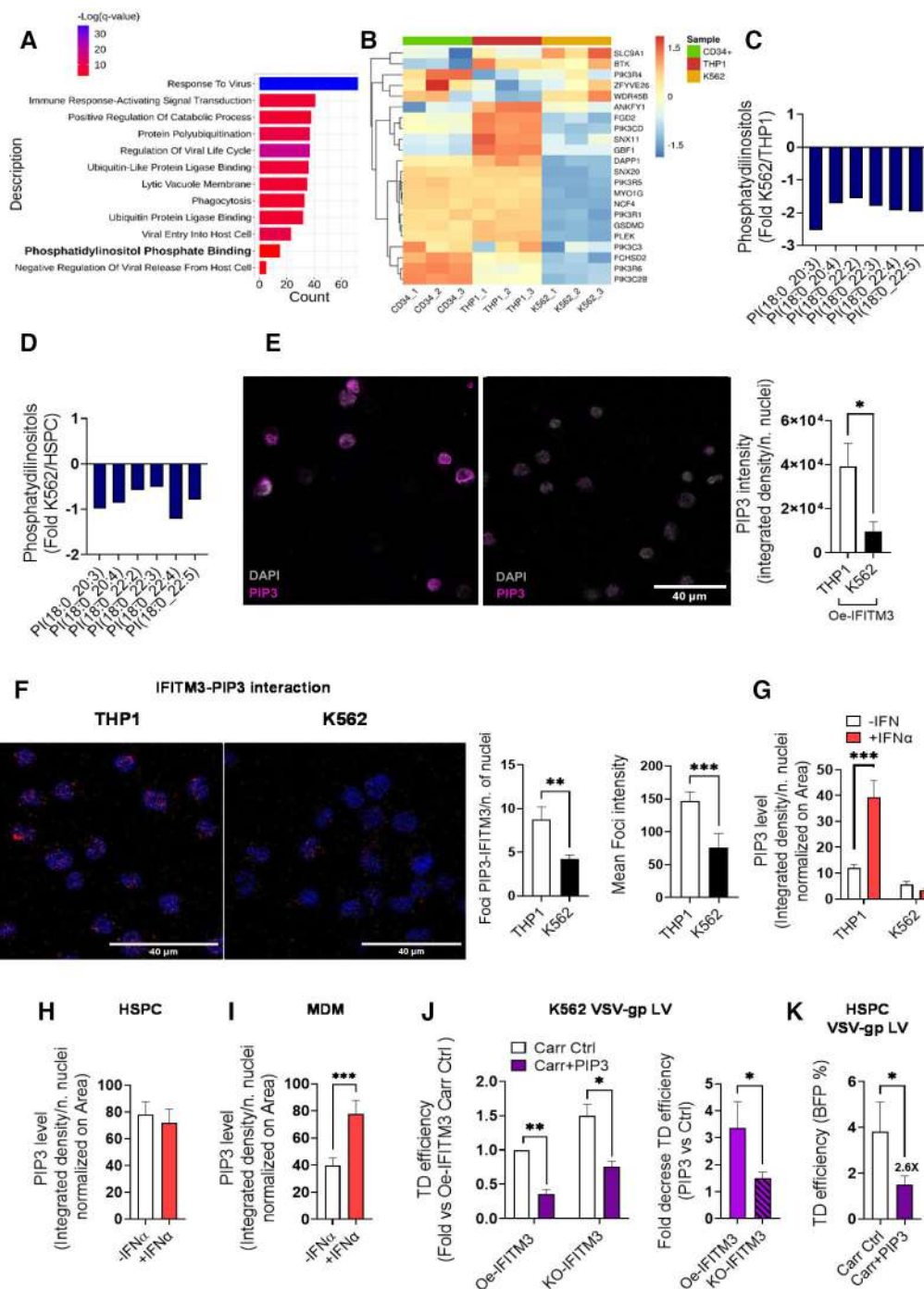


Figure 6.

lysine mutant is still capable of forming dimers but loses capacity to form slower migrating IFITM3 protein complexes. In agreement, comparative proteomics identified distinct interactomes for WT and lysine-less IFITM3. Interactors specific to IFITM3-WT were common to several published datasets related to innate immunity and have been reported to interact with other ISGs, different IFITM3-sensitive viruses as well as with viral ORFs (Pichlmair *et al*, 2012; Mairiang *et al*, 2013; Tripathi *et al*, 2015; Ammari *et al*, 2016; Wang *et al*, 2017; Batra *et al*, 2018; Coyaud *et al*, 2018; Gurumayum

et al, 2018; Hubel *et al*, 2019; Li *et al*, 2019a), strongly supporting their involvement in antiviral immunity. Accordingly, pathways related to antiviral responses and viral transport were among the most significantly enriched. In addition, innate mediators of innate immune signaling such as ubiquitin ligases and phosphatidylinositols (PI) binding proteins, such as Gasdermin A, had significantly higher binding affinity for IFITM3-WT in comparison with the 4KR mutant, suggesting that ubiquitination and phospholipid binding regulate IFITM3 endosomal antiviral activity. In agreement,

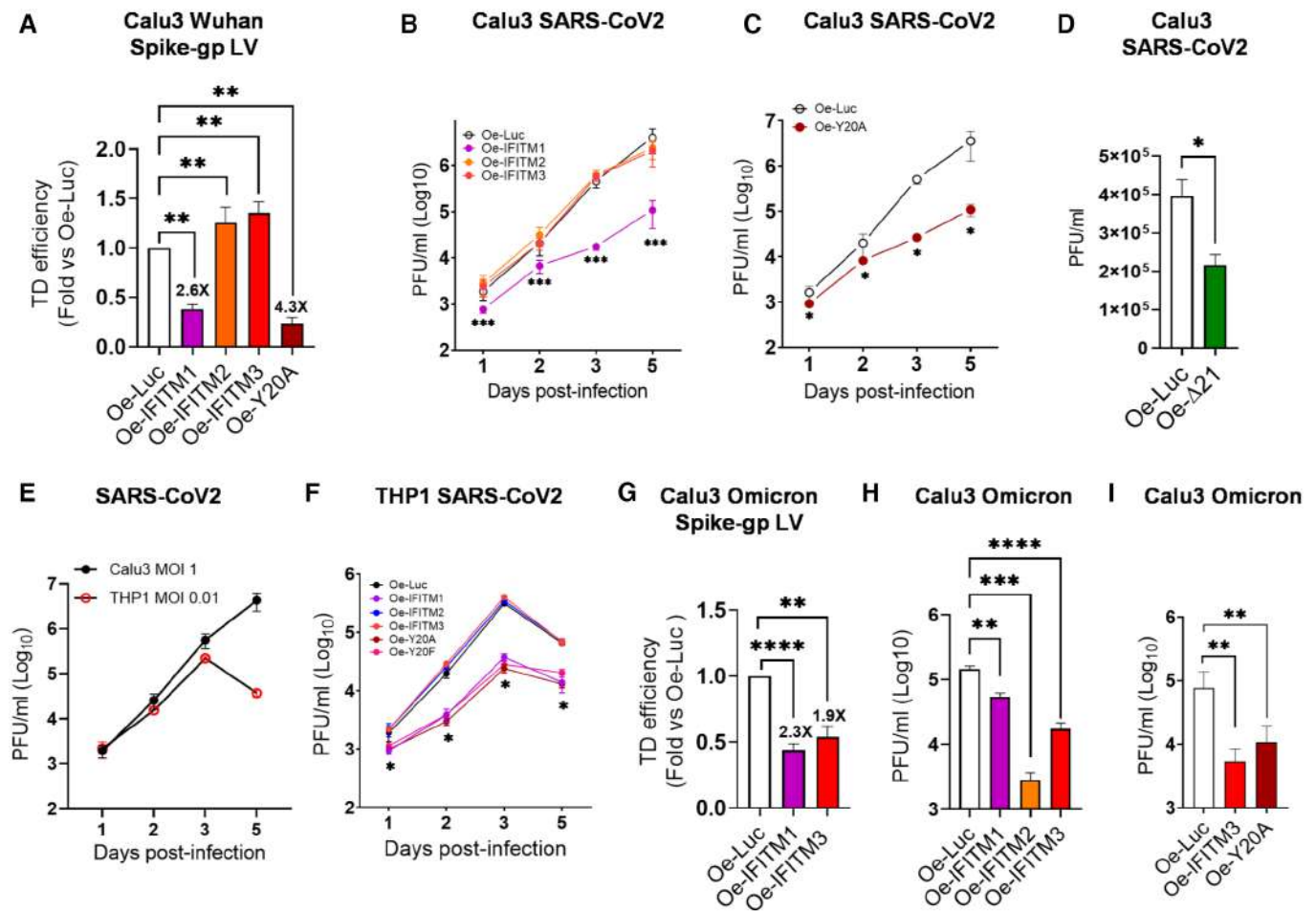


Figure 7. IFITM1 and plasma membrane mutants IFITM3 inhibit SARS-CoV2 entry and infection.

- A** Calu3 overexpressing IFITM1, IFITM2, IFITM3, PM-mutant IFITM3 Y20A, or control were transduced with SARS-CoV2 Spike-pseudotyped LV (mean ± SEM, $n > 6$ biological replicates run in technical duplicate). Transduction efficiency was measured by FACS 5 days after transduction, P -values are for one-sample paired t -test versus Oe-Luc Ctrl = 1, **for $P < 0.01$.
- B, C** Calu3 cells overexpressing IFITM1, IFITM2, IFITM3, IFITM3 Y20A, or control were infected with SARS-CoV2. Viral titer was calculated by plaque assay in Vero E6 cells (mean ± SEM, $n = 4$ biological replicates run in technical duplicate). P -values are for Mann–Whitney test, * for $P < 0.05$, *** for $P < 0.001$.
- D** Calu3 overexpressing IFITM3-Δ21 or control were infected with SARS-CoV2 for 3 days. Viral titer was assessed by plaque assay in Vero E6 cells (mean ± SEM, $n = 3$ biological replicates run in technical duplicate). P -values are for Mann–Whitney test, * for $P < 0.05$.
- E** Calu3 and THP1 were infected with SARS-CoV2 at MOI 1 and 0.01 respectively. Viral supernatant was titered on Vero E6 cells (mean ± SEM, $n = 4$ biological replicates run in technical triplicate).
- F** THP1 cells overexpressing IFITM1, IFITM2, IFITM3, IFITM3 plasma membrane-confined mutants or control were infected with SARS-CoV2 at MOI 0.01. Titers were calculated by titrating viral supernatants on Vero E6 cells (mean ± SEM, $n = 4$ biological replicates run in technical triplicate). P -values are for Mann–Whitney test, * for $P < 0.05$.
- G** Calu3 overexpressing IFITM1, IFITM3, or control were challenged to SARS-CoV2 Omicron-pseudotyped LV. Transduction efficiency was evaluated 5-day post-transduction (mean ± SEM, $n = 7$ biological replicates run in technical duplicate). P -values are for one-sample t -test versus Oe-Luc Ctrl = 1, **for $P < 0.01$, ****for $P < 0.0001$.
- H, I** Calu3 cells overexpressing IFITM1, IFITM2, IFITM3, or control (H) or IFITM3, Y20A, or control (I) were infected with Omicron at MOI 1. Viral supernatants were collected at different time points and titered on Vero E6 cells. Data are presented as mean ± SEM ($n = 4$ –4 biological replicates run in technical triplicate). P -values are for Mann–Whitney test, **for $P < 0.01$, ***for $P < 0.001$, ****for $P < 0.0001$.

we identify Phosphatidylinositol 3,4,5-trisphosphate (PIP3) as a key factor binding the lysine-competent IFITM3 and required for its endosomal but not PM-bound antiviral activity. Phosphoinositide phosphates play an important role in regulating innate immune signal transduction (Barnett & Kagan, 2020). PIP3 and IFITM3 have been recently linked with amplification of PI3K signaling required for B cell activation as well as tumorigenesis (Lee *et al*, 2020) and

PIP3 was shown to regulate Gasdermin D during pyroptosis (Santa Cruz Garcia *et al*, 2022). Moreover, our results suggest that cellular PIP3 content affects endosomal IFITM3 restriction as the IFITM3-insensitive K562 cells harbored lower levels of PIP3 and endosomal restriction could be restored by exogenous PIP3 delivery. PI3K, which acts upstream to Akt/mTOR signaling and converts PIP2 to PIP3 (Vanhaesebroeck *et al*, 2010), has been shown to be

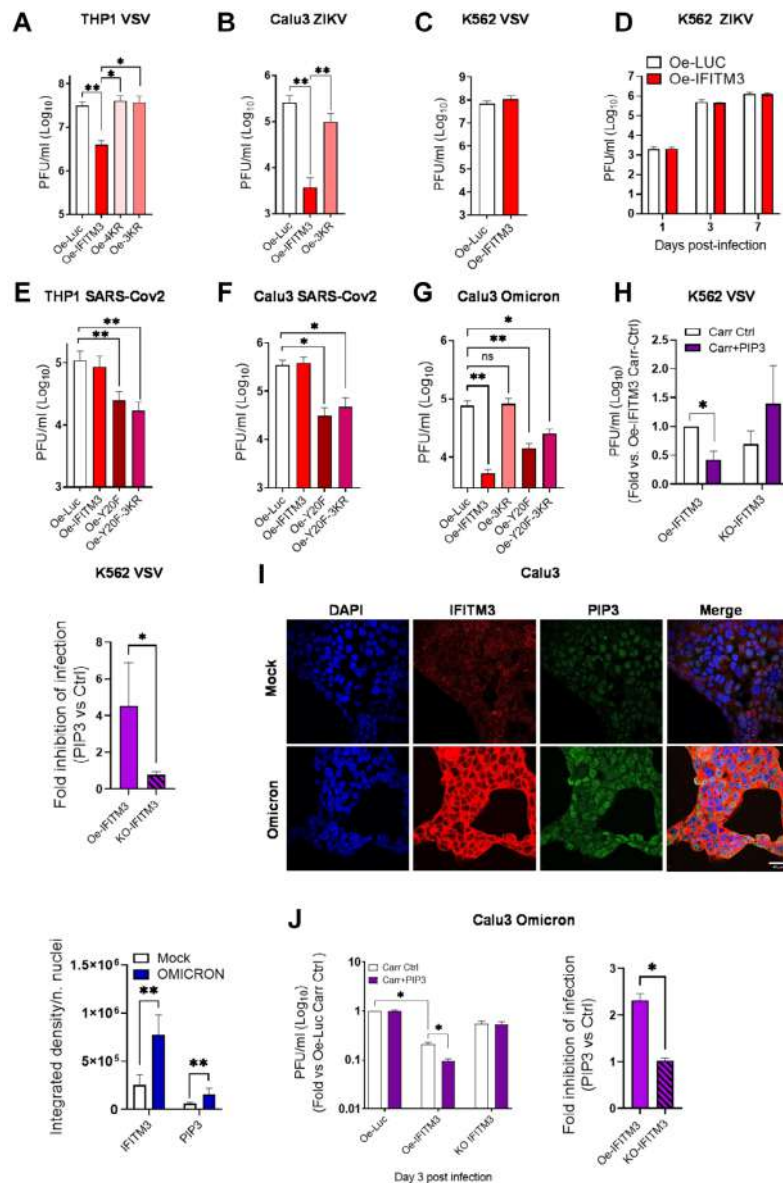


Figure 8. Lysine-dependent PIP3 scaffolding is required for endosomal restriction and can be harnessed to potentiate inhibition of SARS-CoV2 Omicron replication.

- A, B VSV (A) or ZIKV (B) viral supernatants were collected 1-day postinfection in THP1 (A) or Calu3 (B) overexpressing IFITM3, IFITM3 lysine-less mutant (4KR), IFITM3 CIL-lysine mutant (3KR) or control and titered on VERO E6 cells. Data represent the mean \pm SEM ($n = 5-3$ biological replicates run in technical duplicate). P -values are for Mann-Whitney test. * for $P < 0.05$, ** for $P < 0.01$.
- C, D K562 were inoculated with the infectious VSV (C) or ZIKV (D) (mean \pm SEM, $n = 3$ biological replicates run in technical duplicate). Viral supernatant was collected at different time points and titered on Vero E6 cells.
- E-G THP1 (E) or Calu3 (F, G) overexpressing IFITM3, IFITM3-Y20F mutant, IFITM3-Y20F-3KR mutant or control were inoculated with SARS-CoV2 (E, F) or Omicron (G). Viral titers were measured on Vero E6 cells. Data are presented as mean \pm SEM ($n = 4-4-3$ biological replicates run in technical duplicate). P -values are for Mann-Whitney test, * for $P < 0.05$, ** for $P < 0.01$, ns for not significant.
- H K562 overexpressing IFITM3 or KO for IFITM3 were pretreated with PIP3 coupled to a specific PIP carrier (PIP3 + Carr Ctrl) or Carr Ctrl and then infected with VSV. Infectious supernatant were collected after 3 days and titered in Vero E6 cells (mean \pm SEM, $n = 6$ biological replicates run in technical duplicate). P -values are for Wilcoxon signed-ranked test, * for $P < 0.05$. The inhibitory effect of exogenous PIP3 on infection is represented as Fold versus Carr Ctrl (mean \pm SEM, $n = 6$ biological replicates run in technical duplicate). P -values are for Mann-Whitney test, * for $P < 0.05$.
- I IFITM3 and PIP3 levels were measured by immunofluorescence (scale bar 100 μ m) and quantified as integrated density with Imagej software in Calu3 infected or not with Omicron ($n = 3$ biological replicates). P -values are for Mann-Whitney test, ** for $P < 0.01$.
- J PIP3 coupled to a specific PIP carrier (PIP3 + Carr Ctrl) or Carr Ctrl were provided to Calu3 overexpressing IFITM3, control or KO for IFITM3 prior to infection with SARS-CoV2 Omicron. Infectious supernatants were collected after 3 days and titered in Vero E6 cells (mean \pm SEM, $n = 4$ biological replicates run in technical duplicate). P -values are for Wilcoxon signed-ranked test, * for $P < 0.05$. The inhibitory effect of exogenous PIP3 on infection is represented as Fold versus Carr Ctrl (mean \pm SEM, $n = 4$ biological replicates run in technical duplicate). P -values are for Mann-Whitney test, * for $P < 0.05$.

upregulated by type I IFNs (Platanias, 2005). In agreement, we observed that PIP3 is induced by antiviral type I IFN together with IFITM3 in cells competent for endosomal restriction while low levels of either PIP3 or IFITM3 impaired establishment of an effective viral entry block. This suggests that an efficient antiviral state requires sufficient levels of both IFITM3 as well as the IFN-inducible PIP3, establishing a mutual dependency between the two for proficient endosomal restriction. Moreover, PI3K blockade partly lowered IFITM3 antiviral activity and PI3K genes were expressed at lower levels in the IFITM3 insensitive K562 in comparison with THP1 and HSPC, linking lower expression of PI3K genes with cell-type-dependent antiviral effects of IFITM3. Of note, similar mechanisms may apply more broadly to endosomal cargo delivery as increased PIP3 activity was shown to block endocytosis-dependent delivery of nanoparticles (Paunovska et al, 2020), potentially due to enhanced activity of IFITM3 within the endosomal compartment and as IFITM proteins have recently been shown to assist cellular uptake of diverse linked chemotypes (DOI: [10.1126/science.abl5829](https://doi.org/10.1126/science.abl5829)). The Akt/mTOR pathway is a key regulator of several cellular processes, including innate immune responses (Jones & Pearce, 2017). mTOR inhibitors such as Rapamycin were shown to induce IFITM3 degradation and counteract antiviral activity against VSV-gp-pseudotyped LV and Influenza A in HeLa cells (Shi et al, 2018; Ozog et al, 2019), potentially explaining its capacity to enhance LV transduction in human hematopoietic stem cells (HSC; Wang et al, 2014; Petrillo et al, 2015). We confirmed that Rapamycin rescues IFITM3-mediated antiviral activity of VSV-gp-pseudotyped LV and show that it targets endosomal but not plasma membrane restriction by IFITM3. Interestingly, mTORC1 inhibition has been recently shown to trigger membrane phospholipid trafficking to the lysosome for catabolism (Hosios et al, 2022), potentially explaining the effects of Rapamycin on endosomal IFITM3 restriction. In addition, Akt inhibition rescued endosomal IFITM3 restriction, suggesting that the endosomal antiviral mechanism of IFITM3 converges toward the Akt/mTOR pathway through the recruitment of PIP3. In agreement, Akt inhibition has been shown to enhance replication of the IFITM3-sensitive Reovirus in A549 cells (Tian et al, 2015). Our results are also in line with emerging links between SARS-CoV2 and Akt/mTOR signaling pathways as the Akt inhibitor MK-2206 reduces while mTOR overactivation promotes viral replication in Huh-7 cell line and Vero FM (Appelberg et al, 2020; Fattahi et al, 2022). It is tempting to speculate that the effect of MK-2206 on SARS-CoV2 replication is consequent to IFITM3 inhibition and that mTOR inhibitors could be employed to reduce SARS-CoV2 replication.

SARS-CoV2 mainly exploits fusion at the plasma membrane but can enter also through endocytosis (Letko et al, 2020; Scialo et al, 2020; Jackson et al, 2022). So far, controversial results have been reported on the role of IFITMs against SARS-CoV2, with some studies pointing toward a major inhibitory role of IFITM2 (Winstone et al, 2021) or IFITM3 (Zang et al, 2020), others showing antiviral activity from all IFITM (Shi et al, 2021) or even promoting SARS-CoV2 infection (Prelli Bozzo et al, 2021). In our experimental models, IFITM1 seems the most relevant in restricting pre-Omicron SARS-CoV2 variants both in the in context of Spike-pseudotyped vectors as well as infectious viral replication in the naturally permissive lung epithelial Calu3 cells. In addition, IFITM single-nucleotide polymorphisms (SNPs) have been implicated in disease severity of

respiratory infections, including SARS-CoV2 (Everitt et al, 2012; Xu-Yang et al, 2016; Nikoloudis et al, 2020; Zhang et al, 2020), supporting their contribution to diseases progression. We observed that the PM-bound IFITM3-Δ21 mutant isoform, potentially predicted to be encoded by the SNP rs-1225-C (Everitt et al, 2012; Compton et al, 2016; Allen et al, 2017; Randolph et al, 2017; Makvandi-Nejad et al, 2018; Franz et al, 2021), inhibited entry of Spike-gp-pseudotyped LV as well as infectious SARS-CoV2 in Calu3 and THP1 mimicking antiviral activities of IFITM1. Of note, IFITM3 SNP rs-1225-C has been associated with severe Influenza outcomes in Chinese populations (Allen et al, 2017), in line with the endocytic entry route of Influenza viruses. As the Omicron variant of SARS-CoV2 has recently been suggested to favor the endosomal entry route (Pia & Rowland-Jones, 2022; Zhao et al, 2022), it may be differently affected by IFITM SNPs as compared to other variants of concern. Indeed, in line with a localization-dependent antiviral activity of IFITM and its altered viral entry route, the Omicron variant of SARS-CoV2 was most susceptible to restriction by the endosomal IFITM2 and IFITM3, although remaining susceptible also to PM-bound IFITM1 and IFITM3 phosphomutants. Importantly, we observed that exogenous supplementation of PIP3 significantly boosted IFITM3 antiviral activity against the pandemic Omicron variant of SARS-CoV2, rendering PIP3 modulation an attractive strategy to potentiate innate antiviral defenses against emerging infectious pathogens.

Overall, our work uncovers a mechanistic dichotomy between plasma membrane and endosomal antiviral activities of IFITM proteins. We propose that the lysine residues within the intracellular loop of IFITM3 serve as an interaction interface for cellular cofactors with PIP3 playing a central role in its endosomal antiviral activity. These findings inform the development of broadly acting antiviral strategies against IFITM-sensitive viruses, including the current and future pandemic-causing SARS-CoV2 variants. Strategies aimed at modulating cellular PIP3 content have the potential to boost IFITM3 restriction and provide therapeutic benefits in the context of several infectious diseases. Conversely, lowering PIP3 levels could help prevent or counteract malignant transformations and enhance efficacy of several therapeutic strategies that rely on endosomal cargo delivery, including viral vectors and lipid nanoparticles.

Materials and Methods

Vectors

Third-generation LV stocks were prepared, concentrated, and titered as previously described (Dull et al, 1998; Follenzi & Naldini, 2002; Petrillo et al, 2018). Briefly, self-inactivating (SIN) LV vectors were produced using the transfer vector pCCLsin.cPPT.hPGK.eGFP.Wpre, the packaging plasmid pMDLg/pRRE, Rev-expressing pCMV-Rev and the VSV-gp envelope-encoding pMD2.VSV-g plasmids. For pseudotyping LV with the mutant baboon retrovirus envelope, the endogenous feline viral envelope RD114, measles and SARS-CoV2 Spike envelopes, pMD2.VSV-gp was replaced by the BaEV-TR, RD114, measles and Spike envelopes encoding plasmids during vector production as previously described (Frecha et al, 2011; Girard-Gagnepain et al, 2014). The following plasmids encoding SARS-

CoV2 Spike variants were used: pcDNA3.1_spike_del19, generated by deletion of last 19aa of spike starting from pcDNA3.1-SARS2-Spike (a gift from Fang Li, Addgene plasmid # 145032) and is now available to the scientific community through Addgene (Addgene #155297), pcDNA3.1-SARS2-Spike-DEL_D614G was obtained from pcDNA3.1_spike_del19 by insertion of D614G mutation using Quik-Change II XL Site-Directed Mutagenesis Kit (Agilent), pcDNA3.1-SARS2-Spike-B.1.1.7_DEL, pcDNA3.1-SARS2-Spike-B.1.351_DEL, and pcDNA3.1-SARS2-Spike-B.1.351 were obtained from pcDNA3.1_spike_del19 by GeneScript mutagenesis service. The bidirectional LV (Amendola *et al*, 2013) were used to overexpress the coding sequence (CDS) of candidate human genes under the control of the human phosphoglycerate kinase (PGK) promoter and the eGFP and the minimal cytomegalovirus (mCMV) promoter forming the antisense expression unit. Bidirectional transfer plasmid for overexpression of IFITM3 was made by cloning IFITM3 cDNA sequence into BamHI and XmaI sites. IFITM3 and IFITM1 mutants were made either by site-directed mutagenesis PCR or designed and then synthesized by Twin-Helix (specifically IFITM3-4KR, IFITM3-3KR, IFITM3-Δ21, IFITM1-3KR, and IFITM3-dimerization mutant). KO experiments were performed using lentiCRISPR v2, which encode both Cas9 and RNA guides against the gene of interest as previously described (Petrillo *et al*, 2018).

Cells

Cell lines

The human embryonic kidney 293T (HEK293T) and K562 cells were maintained in Iscove's modified Dulbecco's medium (IMDM; Sigma); human THP1 cells were maintained in Roswell Park Memorial Institute medium (RPMI; Lonza). All media were supplemented with 10% fetal bovine serum (FBS; Gibco), penicillin (100 IU/ml), streptomycin (100 µg/ml), and 2% glutamine. A549 and Vero E6 cells were cultured in Dulbecco's Modified Eagle Medium (DMEM, Sigma) supplemented with 10% fetal bovine serum (FBS; Gibco), 1% Nonessential amino acid (NEAA, Gibco), 1% Sodium Pyruvate (Gibco). Calu3 were cultured in Dulbecco's Modified Eagle Medium (DMEM, Sigma) supplemented with 20% fetal bovine serum (FBS; Gibco), 1% Nonessential amino acid (NEAA, Gibco), 1% Sodium Pyruvate (Gibco) and 2% GlutaMAX (Gibco). All cells were maintained in a 5% CO₂ humidified atmosphere at 37°C. A549-hACE2 cell lines were generated by lentiviral transduction. Lentiviral vectors were produced following a standard procedure based on calcium phosphate co-transfection with 3rd-generation helper and transfer plasmids.

Primary cells

Human CD34⁺ HSPC were isolated through positive magnetic bead selection according to the manufacturer's instructions (Milteny) from umbilical cord blood or from mononuclear cells collected upon informed consent from healthy volunteers according to the Institutional Ethical Committee approved protocol (TIGET01). Otherwise, CB, bone marrow (BM) or G-CSF mPB-CD34⁺ cells were directly purchased from Lonza or Hemacare. All cells were maintained in a 5% CO₂ humidified atmosphere at 37°C.

Transduction

All cells were transduced at the indicated multiplicity of infection (MOI) as calculated by titration of vector stocks on 293T cells and

expressed as transducing units (TU)/293T cell. Cell lines were transduced with LV for 16 h, washed, and kept in culture until reading transduction efficiency by flow cytometry. Human CB-derived HSPC were cultured in serum-free StemSpan medium (StemCell Technologies) supplemented with penicillin (100 IU/ml), streptomycin (100 µg/ml), 100 ng/ml recombinant human stem cell factor (rhSCF), 20 ng/ml recombinant human thrombopoietin (rhTPO), 100 ng/ml recombinant human Flt3 ligand (rhFlt3), and 20 ng/ml recombinant human IL6 (rhIL6; all from Peprotech) 16–24 h prior to transduction. HSPC were then transduced at a concentration of 1×10^6 cells per milliliter with VSV-gp-pseudotyped SINLV for 16 h at the indicated multiplicity of infection (MOI) in the same medium. G-CSF mobilized peripheral blood CD34⁺ cells were maintained in culture in CellGro medium (Cell Genix) containing a cocktail of cytokines: 60 ng/ml IL-3, 100 ng/ml TPO, 300 ng/ml SCF, and 300 ng/ml FLT-3L (all from Cell Peprotech). Transductions were performed with the indicated dose of vectors for 16 h in the same cytokine-containing medium. For single-hit reporter LV transductions, cells were washed and maintained in serum-free medium supplemented with cytokines as above until the reading of the percentage of positive cells by FACS. To perform OE, KD, and KO experiments, cells were transduced with the respective LV and then challenged with a second transduction with or without drugs. Except for primary cells, KD and KO cells were selected with Puromycin before the second hit of transduction.

Transduced cells

GFP or BFP expression was measured 5-day post-transduction in cells transduced with LV or 16 h after Spike-pseudotyped VSV infection. Calu3 cells were detached using Trypsin-EDTA (Sigma), washed, and resuspended in PBS containing 2% FBS. Cells grown in suspension were washed and resuspended in PBS containing 2% FBS. 7-aminoactinomycin D (Sigma-Aldrich) was included during sample preparation according to the manufacturer's instructions to identify dead cells.

Flow cytometry

All cytometric analyses were performed using the FACSCanto III instrument and Cytoflex S instruments (BD Biosciences) and analyzed with the FACS Express software (*De Novo* Software).

Viral infection

All infections with SARS-CoV2 viral strains have been performed under appropriate BSL3 biosafety level containment by trained personnel, in agreement with Italian regulations (art. 269 del D. Lgs. 81/80, protocol nr. 39 authorized 11.02.2022).

Calu-3 infection with SARS-CoV 2

Calu-3 cells were plated at 5×10^4 cell/well in 48-well plates in DMEM supplemented with 5% fetal bovine serum (FBS; complete medium). Twenty-four hours later, SARS-CoV-2 isolate (GISAID accession ID: EPI_ISL_413489) was added at multiplicity of infection (MOI) of 1 in a final volume of 150 µl of medium supplemented with 2% FBS. The cells were inoculated for 1 h, and then the inoculi were removed. Five hundred microliter of complete medium was added. Cell culture supernatants were collected at different time points postinfection and stored at –80°C until determination of the

viral titers by a plaque-forming assay in Vero E6 cells and retrotitration.

THP1 infection with SARS-CoV 2

THP1 cells were plated at 1×10^5 cell/well in 48-well plates in 100 μ l in RPMI supplemented with 2% fetal bovine serum (complete medium). After seeding, SARS-CoV-2 isolate (GISAID accession ID: EPI_ISL_413489) was added at a multiplicity of infection (MOI) of 0.01. The virus was let adsorb for 1 h, and then 400 μ l of RPMI supplemented with 2% serum was added. Cell culture supernatants were collected at different time points and stored at -80°C until determination of the viral titers by a plaque-forming assay in Vero E6 cells.

Calu-3 infection with Zika virus (ZIKV)

Calu-3 cells were plated at 5×10^4 cell/well in 48-well plates in DMEM supplemented with 5% fetal bovine serum (FBS; complete medium). Twenty-four hours later, Zika virus PRVABC59 strain (GenBank Accession #KU501215) was added at multiplicity of infection (MOI) of 0.1 in a final volume of 150 μ l of medium supplemented with 2% FBS. After 2 h of infection, inoculi were removed and 500 μ l of complete medium was added. Cell culture supernatants were collected at 72-h postinfection and stored at -80°C until determination of the viral titers by a plaque-forming assay in Vero E6 cells and retrotitration.

K562 infection with Zika virus (ZIKV)

K562 cells were plated at 1×10^5 cell/well in 48-well plates in IMDM supplemented with 2% fetal bovine serum (FBS; complete medium). Twenty-four hours later, Zika virus PRVABC59 strain (GenBank Accession #KU501215) was added at multiplicity of infection (MOI) of 0.1 in a final volume of 150 μ l of medium supplemented with 2% FBS. After 2 h of infection, inoculi were removed and 500 μ l of complete medium was added. Cell culture supernatants were collected at 72-h postinfection and stored at -80°C until determination of the viral titers by a plaque-forming assay in Vero E6 cells and retrotitration.

Plaque-forming assay

In order to measure the virus titer of viral stocks of SARS-CoV-2 (GISAID accession ID: EPI_ISL_413489) and ZIKV PRVABC59 strain (GenBank Accession #KU501215), a plaque-forming assay was optimized in Vero E6 cells. Briefly, confluent Vero cells (1.5×10^6 cell/well) seeded in 6-well plates (Corning) were incubated in duplicate with 1 ml of EMEM supplemented with 1% FBS containing 10-fold serial dilutions of SARS-CoV-2 stock. After either 1 h (SARS-CoV-2) or 2 h (ZIKV) of incubation, the viral inoculum was removed and methylcellulose (Sigma; 1 ml in EMEM supplemented with 1% FBS) was overlaid on each well. After 4 or 6 days of SARS-CoV-2 and ZIKV incubation, respectively, the cells were stained with 1% crystal violet (Sigma) in 70% methanol. The plaques were counted after examination with a stereoscopic microscope (SMZ-1500; Nikon Instruments) and the virus titer was calculated in terms of plaque-forming units (PFU)/ml.

In order to determine the viral titers of the supernatants collected from Calu-3 and THP1 cells, confluent Vero cells (2.5×10^5 cell/well) were seeded in 24-well plates (Corning) 24 h prior to infection. Then, cells were incubated with 300 μ l of EMEM supplemented

with 1% FBS containing serially diluted (1:10) virus-containing supernatants. The plaque-forming assay was performed as described above.

Compounds

Rapamycin (Sigma-Aldrich), MK2206 (SelleckChem), LY294002 (Cell signaling), and Amphotericin B (Sigma-Aldrich) were resuspended and stored following the manufacturer's instructions. Rapamycin was added to the transduction medium at concentration of 8 and 10 μM concomitantly with transduction, MK2206 was added 1 h prior transduction at concentration of 2 μM , LY294002 was added 24 h before transduction at concentration of 25 μM , and Amphotericin B was added 1 h prior transduction at 1 μM concentration as in (Lin et al, 2013; Rahman et al, 2020). A wash was performed 16 or 20 h later. Human IFN α (from pbl assay science 11105-1) prestimulation was performed for 24 h at the indicated concentration.

Exogenous delivery of PIP3

Phosphatidylinositol 3,4,5-trisphosphate diC16 (Echelon Biosciences 117P-3916) was freshly reconstituted with PBS at 2 mM. Unlabelled shuttle PIP carrier 2 (histone H1) was freshly reconstituted with water at 2 mM as per manufacturer instructions (Echelon Biosciences 117P-9C2-1ea). 0.75 μ l of PIP3 was mixed to 0.25 μ l of PIP carrier and incubated at room temperature for 10 min. 5×10^4 K562 cells concentrated at 1×10^6 /ml were exposed to 1 μ l of PIP3-carrier complex for 30 min prior to transduction.

RNA extraction, qPCR and gene expression analysis

RNA extraction from cells was performed using the RNeasy micro Kit or RNeasy Plus micro Kit (QIAGEN) or ReliaPrep RNA Cell Mini-prep System (Promega). Briefly, cells were lysed in Buffer RLT plus, supplemented with beta-mercaptoethanol. RNA was then extracted according to manufacturer's instructions. The extracted mRNAs were reverse transcribed (RT) using the SuperScript Vilo kit (11754-250; Invitrogen). RT-qPCR analyses were performed using TaqMan probes from Applied Biosystems to detect endogenous mRNA levels. Otherwise, we designed specific primers to quantify the overexpression of the coding sequence of human IFITM2 and IFITM3 genes (see table). Q-PCR was run for 40 cycles using the Viia 7 instrument, while the Viia 7 software was then used to extract the raw data (Ct). To determine gene expression, the difference (ΔCt) between the threshold cycle (Ct) of each gene and that of the reference gene was calculated by applying an equal threshold. Relative quantification values were calculated as the fold-change expression of the gene of interest over its expression in the reference sample, by the formula $2^{-\Delta\Delta\text{Ct}}$. The expression was normalized using the housekeeping gene HPRT1 or GAPDH. Human Taqman probes from Applied Biosystems were used and reported in Key resource table.

Western blot

Whole-cell extracts were prepared as previously described (Kajaste-Rudnitski et al, 2006, 2011). Samples were subjected to SDS-PAGE using Bolt 4–12% Bis-Tris Plus Gels (Thermo Fisher Scientific), transferred to PVDF membrane by electroblotting, and blotted with rabbit anti-IFITM3 polyclonal Ab (1:1,000 dilution, proteintech Cat# 11714-1-AP); rabbit anti-IFITM2 polyclonal Ab (1:2,500, proteintech Cat# 12769-1-AP); mouse anti-IFITM1 monoclonal Ab (1:5,000,

proteintech Cat# 60074-1-Ig), rabbit anti-ACE2 (1:1,000, Cell Signaling Technology 4355S), rabbit anti-HA tag antibody—ChIP Grade (1:10,000 Abcam Cat# ab9110), mouse anti-his (1:10,000 Millipore Cat# 05-909). A mouse monoclonal anti-beta-actin Ab (1:10,000 dilution, Sigma-Aldrich Cat# A2228) was used as a normalizer. After the incubation with primary antibodies, PVDF membranes were washed three times with tris-buffered saline (TBS) 0.1% tween 20 for 5 min and then incubated for 1 h with rabbit or mouse IgG secondary antibodies (1:10,000; GE Healthcare Cat# NA934, GE Healthcare Cat# NA931).

Native PAGE

For native protein extraction, 3×10^5 cells were pelleted for each condition. Cells were lysed in Native Lysis Buffer (50 mM Tris-HCl pH 7.5, 150 mM NaCl, 1 mM EDTA, 1% NP-40) in the presence of Protease cocktail inhibitor (cOmplete™, EDTA-free Protease Inhibitor Cocktail, Sigma-Aldrich, catalog number 11873580001). Protein lysates were left rotating on-wheel at 4°C for 15 min and cleared by 15 min of centrifugation at 4°C at 13,200 (max speed). Protein supernatants were transferred in new empty tube and quantified as previously described (Kajaste-Rudnitski *et al*, 2006, 2011). For Native PAGE, 7% Running native gel and 4% Stacking native gel were prepared. Before running the native protein samples, the inner electrophoretic chamber was filled with fresh Native Running Buffer (25 mM Tris, 192 mM Glycin, pH 8.4) with 1% of Deoxycholate (DOC) and the outer chamber with Native Running Buffer without DOC and the gel was run empty at 4°C for 30 min at 40 mA. 20–40 µg of protein diluted in native sample buffer $3 \times$ (187.5 mM Tris-HCl, 45% Glycerol, 3% DOC, and Bromophenol blue) were run at 4°C for 5 h at 15 mA. Samples were transferred to a Nitrocellulose membrane by electroblotting and blotted with rabbit anti-IFITM3 polyclonal Ab (1:1,000 dilution, from proteintech catalog number 11714-1-AP), anti-Vinculin (1:20,000 dilution Millipore) or anti-beta-actin Ab (1:10,000 dilution, Sigma-Aldrich Cat# A2228) were used as a normalizer. After the incubation with primary antibodies, membranes were washed three times with tris-buffered saline (TBS) 0.1% tween 20 for 5 min and then incubated for 1 h with rabbit or mouse IgG secondary antibodies (1:10,000; GE Healthcare Cat# NA934, GE Healthcare Cat# NA931).

Immunoprecipitation

For immunoprecipitation of IFITM 3.5–10 million cells were lysed in RIPA-NP-40 buffer with Phosphatase inhibitor cocktail (PHOSSTOP, Roche, catalog number 04906837001) and protease inhibitor cocktail (cOmplete™, EDTA-free Protease Inhibitor Cocktail, Sigma-Aldrich, catalog number 11873580001). Dynabeads™ Protein G for Immunoprecipitation (Life Technologies catalog number 100007D) were prepared according to the manufacturer's instructions. Ten microgram of rabbit anti-IFITM3 Ab (from proteintech Cat# 11714-1-AP) or anti-mouse IgG control were added to the beads and left in incubation for an O/N with rotation. After cross-linking of the antibody to the Dynabeads (Thermo Fisher reagents Cat# 21580), 1 mg of proteins lysate was mixed to the Dynabeads-Ab complex. After an O/N incubation in rotation at 4°C, beads were washed according to the manufacturer's instructions. IFITM3 and IgG control were eluted with elution buffer premixed with NuPAGE LDS Sample Buffer (Thermo Scientific catalog number B0007) and

NuPAGE samples Reducing Agent (Thermo Scientific catalog number B0009) and examined with Western blotting by standard procedures.

Mass spectrometry

The entire lanes were excised from the SDS-gel and cut into small pieces. Proteins' disulfide bridges were reduced by using 10 mM DTT in 100 mM NH_4HCO_3 at 56°C for 55 min and successively alkylated by using 55 mM iodoacetamide in 100 mM NH_4HCO_3 for 20 min at the room temperature. Proteins were digested with trypsin (0.1 µg/µl in 100 mM NH_4HCO_3) and incubated at 37°C overnight. After digestion, peptides were extracted from the gel pieces using 95% acetonitrile and 5% formic acid. Extracted peptides were dried and purified using the StageTip procedure (Rappsilber *et al*, 2003). Digested samples were injected onto a quadrupole Orbitrap Q-exactive HF mass spectrometer (Thermo Scientific). Peptide separation was achieved on a linear gradient from 95% solvent A (2% ACN, 0.1% formic acid) to 55% solvent B (80% acetonitrile, 0.1% formic acid) over 42 min and from 55 to 100% solvent B in 3 min at a constant flow rate of 0.25 µl/min on UHPLC Easy-nLC 1000 (Thermo Scientific) where the LC system was connected to a 23-cm fused-silica emitter of 75 µm inner diameter (New Objective, Inc. Woburn, MA, USA), packed in-house with ReproSil-Pur C18-AQ 1.9 µm beads (Dr Maisch GmbH, Ammerbuch, Germany) using a high-pressure bomb loader (Proxeon, Odense, Denmark). The mass spectrometer was operated in DDA mode as described previously (Matafora *et al*, 2017). Dynamic exclusion enabled (exclusion duration = 15 s), MS1 resolution = 70,000, MS1 automatic gain control target = 3×10^6 , MS1 maximum fill time = 60 ms, MS2 resolution = 17,500, MS2 automatic gain control target = 1×10^5 , MS2 maximum fill time = 60 ms, and MS2 normalized collision energy = 25. For each cycle, one full MS1 scan range = 300–1,650 m/z was followed by 12 MS2 scans using an isolation window of 2.0 m/z. All raw files were processed using MaxQuant (Cox & Mann, 2008; Version 1.6.0.16) against a uniprot-complete proteome_HomoSapiens_2019_database where the sequence of 4KR mutant IFITM3 was added. Carbamidomethylation was set as fixed modification while methionine oxidation and N-terminal acetylation were searched as variable modifications. Statistical analysis was done in Perseus (Tyanova *et al*, 2016) using two-sample *t*-test with Benjamini–Hochberg correction set at FDR < 0.05.

Immunofluorescence microscopy

5×10^4 THP1, K562 or CB3D34⁺ cells were seeded in Multitest slide glass 10-well 8 mm (from MP Biomedicals) precoated with poly-L-lysine solution (Sigma-Aldrich) for 20 min while Calu3 were seeded in multitest slide glass 10-well 8 mm (from MP Biomedicals) 1 day before fixation. Cells were fixed with 4% paraformaldehyde (in 1× PBS) for 20 min at room temperature, washed with 1× PBS, and permeabilized with 0.1% Triton X-100 for 20 min at room temperature. For blocking nonspecific sites cells were incubated 30 min in PBG (5% BSA, 2% gelatin from cold water fish skin, from Sigma-Aldrich) and then stained for 2 h at room temperature or 16 h at 4°C with rabbit anti-IFITM3 polyclonal antibody (1:200 dilution from proteintech catalog number 11714-1-AP), rabbit anti-IFITM2 polyclonal Ab (1:200, proteintech Cat# 12769-1-AP); mouse anti-IFITM1 monoclonal Ab (1:100, proteintech Cat# 60074-1-Ig), rabbit

anti-ACE2 (1:100, Cell Signaling Technology 4355S), rabbit anti hTMPRSS2 (1:200, Sino Biological Cat#204314-T08), mouse anti-LAMP1 monoclonal antibody (1:100 dilution from Abcam [H4A3] (ab25630)), goat anti-LAMP1 (1:100 dilution from Abcam cat#ab2245). After three washes with 1× PBS, cells were incubated with donkey anti-Rabbit IgG, AlexaFluor 488 or 555 (1:500 dilution from ThermoFisher Scientific Cat# A-21206, A-31572), anti-mouse IgG, AlexaFluor 647 (1:500 dilution from Thermo Fisher Scientific catalog number A-31573) and anti-goat IgG, AlexaFluor 647 (1:500 dilution from Abcam catalog number Ab150155) for 1–2 h at room temperature. Nuclei were stained with DAPI (4',6-diamidino-2-phenylindole; 10236276001, Roche, Basel, Switzerland) for 5 min at room temperature. Images were recorded using the TCS SP5 Leica confocal microscope, 60× with oil.

Proximity ligation assay

Proximity ligation assay was performed using the Duolink PLA Fluorescence protocol following manufacturer's instructions. In brief, 5×10^4 THP1 or K562 were seeded in Multitest slide glass 10-well 8 mm (from MP Biomedicals) precoated with poly-L-lysine solution (Sigma-Aldrich) for 20 min. Cells were fixed with 4% paraformaldehyde (in 1× PBS) for 20 min at room temperature, washed with 1× PBS and permeabilized with 0.2% Triton X-100 for 30 min at room temperature. Blocking was performed for 1 h. After a wash with PBS cells were incubated for 16 h at 4°C with rabbit anti-HA tag antibody - ChIP Grade (1:1,000 Abcam Cat# ab9110), mouse anti-his (1:1,000 Millipore Cat# 05-909), mouse Purified Anti-PtdIns(3,4,5) P3 IgG (Echelon Cat# Z-P345B-2). A step of PLA probe incubation, ligation, and amplification were followed according to the manufacturer's instructions. After some washing steps, slide was mounted and PLA foci were recorded using the TCS SP5 Leica confocal microscope, 60× with oil.

Bioinformatic analysis

IFITM3 sequences alignment

IFITM3 protein sequences from other species were collected from orthologues of the human IFITM3 gene using gene annotations from the RefSeq database including representative species from mammals, birds, and fish. The Refseq protein accessions were used to retrieve the amino acid sequences of the proteins from the different species analyzed: NP_001185686.1 (*Pan troglodytes*), NP_079654.1 (*Mus musculus*), NP_001129596.1 (*Rattus norvegicus*), NP_001188311.1 (*Sus scrofa*), NP_001071609.1 (*Bos taurus*), NP_001336988.1 (*Gallus gallus*), and NP_001170783.1 (*Danio rerio*). Alignment of the amino acid sequences was performed using the Clustal Omega tool (version 1.2.4) with default settings (Sievers et al, 2011). Protein domains were retrieved using the InterPro database (Hunter et al, 2009). The multiple sequence alignment and the protein domains were then viewed and edited using Jalview (version 2) alignment software (Waterhouse et al, 2009). Residue conservation was calculated as a numerical index reflecting the conservation of physicochemical properties for each column of the alignment as previously described (Livingstone & Barton, 1993). Conservation is visualized on the alignment or as a histogram giving the score for each column. Conserved columns have the highest score and are indicated by a "*", and columns with mutations where all properties are conserved are marked with a "+".

RNA sequencing

Total RNA was extracted with the RNeasy Plus Micro kit (Qiagen) according to the manufacturer's indications. RNA integrity was analyzed with the Agilent 2100 Bioanalyzer (Agilent Technologies, Santa Clara, CA). Libraries, prepared starting from 100 ng of total RNA/sample with the Illumina TruSeq RNA Sample Prep kit v2 procedure, were quantified by the Qubit BR assay (Life Technologies, Illkirch, France) and the Agilent 2100 Bioanalyzer. Sequencing was performed on the Illumina HiSeq 2500 platform using SBS 2x100PE protocol. Short reads were aligned to hg19 reference genome using STAR aligner (v 2.4; Dobin et al, 2013). Genes were quantified using Rsubread package (Liao et al, 2019) using GENCODE v19 gene definition (Harrow et al, 2012). Counts were normalized using TMM approach (Oshlack et al, 2010), and genes with less than 1 count per million in at least three samples were excluded from the analysis. Differential gene expression analysis was performed by the R/Bioconductor packages DESeq2 (Love et al, 2014) comparing responder (CD34⁺ and THP1 cells) versus nonresponder cells (K562 cells). Genes with adjusted *P*-values < 0.05 were considered differentially expressed. A functional enrichment analysis of Gene Ontology (GO) terms was performed on the lists of significantly upregulated differentially expressed genes using the R/Bioconductor package clusterProfiler (Wu et al, 2021) version 4.2.1. Enriched terms with an adjusted *P*-value < 0.05 were considered statistically significant. Heatmaps were generated using the R package pheatmap (<https://CRAN.R-project.org/package=pheatmap>).

MS analysis

Gene ontology (GO) enrichment analysis was performed on the list of differentially interacting genes upregulated in IFITM3-WT in comparison with 4KR-IFITM3 using the R/Bioconductor package clusterProfiler (Wu et al, 2021) version 4.2.1. Enrichment *P*-values were corrected for multiple testing using FDR and considered statistically significant if less than 0.05. Heatmap was generated using R/Bioconductor package ComplexHeatmap (Gu et al, 2016) version 2.0.0.

The list of IFITM3-WT upregulated interactors and their corresponding functional terms identified at the previous step was imported into Cytoscape (version 3.9.0; <http://www.cytoscape.org>; Shannon et al, 2003) for network visualization. The significant terms were clustered into functional modules, and the connectivity among related terms was constructed using Jaccard similarity coefficients; the edge thickness is proportional to the Jaccard coefficient between one term and all the other terms.

Lipidomics

For untargeted lipidomics analyses, samples were processed as described, over an ACQUITY HSS T3 column and high-resolution MS2 analyses via a Vanquish UHPLC coupled to a Q-Exactive orbitrap instrument (Thermo Fisher, Bremen, Germany).

Intersecting IFITM3 interactors with public data

IFITM3-WT interactors identified in the previous step were intersected with public datasets considering the following viral interactome datasets: Zika virus (Coyaud et al, 2018; Gurumayum et al, 2018); Influenza virus (Tripathi et al, 2015; Wang et al, 2017), West Nile virus (Li et al, 2019b), Hepatitis C virus (HCV; Kwofie et al, 2011), Dengue virus (Mairiang et al, 2013), and Ebola virus

(Batra *et al*, 2018), a curated database for host–pathogen interactions HPIDB version 3.0 (Ammari *et al*, 2016), ISG interactors (Hubel *et al*, 2019) and identified vORF targets (Pichlmair *et al*, 2012). Interactors from different datasets were mapped using ENSEMBL database to the UniProt accession codes of reviewed human protein sequences. Significance of the overlap between one of the defined groups and the external sets was determined by Fisher's exact test and against the remaining human proteome background. Venn diagrams were generated using R package VennDiagram (Chen & Boutros, 2011) version 1.6.20. Barplot was produced using R package ggplot2.

Statistical analysis

All statistical analyses were conducted with GraphPad Prism 9 version. In all studies, values are expressed as mean \pm standard error of the mean (SEM) and all *n* numbers represent biological repeats. Statistical analyses were performed as indicated in the figure legends. For WB quantifications, signal was quantified by densitometry using the ImageJ software and normalized to actin. For IF quantification, signal was measured using the ImageJ software and normalized to number of cells. *n* represents the number of biological replicates performed. Differences were considered statistically significant at **P* < 0.05, ***P* < 0.01, ****P* < 0.001, *****P* < 0.0001, “ns” represents nonsignificance.

Data availability

RNA-seq data have been deposited to ArrayExpress (<https://www.ebi.ac.uk/biostudies/arrayexpress>) with the following accession number: E-MTAB-6598 (<http://www.ebi.ac.uk/arrayexpress/experiments/E-MTAB-6598>). Lipidomics datasets have been deposited to Metabolomics Workbench and assigned the study ID ST002413 (<https://www.metabolomicsworkbench.org/data/DRCCMetadata.php?Mode=Study&StudyID=ST002413>). Proteomics data have been deposited to the PRIDE repository, project accession: PXD038896 (<https://www.ebi.ac.uk/pride/archive?keyword=PX038896>).

Expanded View for this article is available [online](#).

Acknowledgements

This work was supported by grants from the European Research Council (ERC-CoG 819815-ImmunoStem), The Italian Ministry of Health (GR-2018-12366006) and the Telethon Foundation (TELE20-C3) to KRA. UG and CG conducted this study as partial fulfillment of their Ph.D. in Molecular Medicine, Program in Cellular and Molecular Physiopathology, International Ph.D. School, Vita-Salute San Raffaele University, Milan, Italy. We wish to thank Andy Wang for technical help with plasmid cloning, Cesare Covino from Alembic for the help with the confocal imaging acquisition and analysis, Luigi Naldini and Florian Douam for critical reading of the manuscript. Open access funding provided by BIBLIOSAN.

Author contributions

Giulia Unali: Conceptualization; data curation; formal analysis; methodology; writing – original draft; writing – review and editing. **Giovanni Crivichic:** Data curation; formal analysis; methodology. **Isabel Pagani:** Data curation;

formal analysis; methodology. **Monah Abou-Alezz:** Data curation; formal analysis; methodology; writing – original draft. **Filippo Folchini:** Formal analysis; methodology. **Erika Valeri:** Formal analysis; methodology. **Vittoria Matafora:** Data curation; formal analysis; methodology; writing – original draft. **Julie A Reisz:** Data curation; formal analysis; methodology; writing – original draft. **Anna Maria Sole Giordano:** Data curation; formal analysis; methodology. **Ivan Cuccovillo:** Formal analysis; methodology. **Giacomo M Butta:** Methodology. **Lorena Donnici:** Resources; methodology. **Angelo D'Alessandro:** Conceptualization; data curation; supervision; writing – original draft. **Raffaele De Francesco:** Resources; methodology. **Lara Manganaro:** Resources; methodology. **Davide Cittaro:** Data curation; formal analysis; writing – original draft. **Ivan Merelli:** Conceptualization; data curation; supervision; writing – original draft. **Carolina Petrillo:** Conceptualization; supervision; writing – original draft. **Angela Bachi:** Data curation; supervision; writing – original draft. **Elisa Vicenzi:** Data curation; supervision; writing – original draft. **Anna Kajaste-Rudnitski:** Conceptualization; data curation; formal analysis; supervision; funding acquisition; investigation; writing – original draft; project administration; writing – review and editing.

Disclosure and competing interests statement

The authors declare that they no conflict of interest.

References

- Alem A, Akbar Samad AB, Slenker AK (2022) *Emerging variants of SARS-CoV-2 and novel therapeutics against coronavirus (COVID-19)*. Treasure Island, FL: StatPearls
- Allen EK, Randolph AG, Bhargava T, Dogra P, Ohlson M, Oshansky CM, Zamora AE, Shannon JP, Finkelstein D, Dressen A *et al* (2017) SNP-mediated disruption of CTCF binding at the IFITM3 promoter is associated with risk of severe influenza in humans. *Nat Med* 23: 975–983
- Amendola M, Giustacchini A, Gentner B, Naldini L (2013) A double-switch vector system positively regulates transgene expression by endogenous microRNA expression (miR-ON vector). *Mol Ther* 21: 934–946
- Amini-Bavil-Olyaei S, Choi YJ, Lee JH, Shi M, Huang IC, Farzan M, Jung JU (2013) The antiviral effector IFITM3 disrupts intracellular cholesterol homeostasis to block viral entry. *Cell Host Microbe* 13: 452–464
- Ammari MG, Gresham CR, McCarthy FM, Nanduri B (2016) HPIDB 2.0: a curated database for host–pathogen interactions. *Database (Oxford)* 2016: baw103
- Appelberg S, Gupta S, Svensson Akusjarvi S, Ambikan AT, Mikaeloff F, Saccon E, Vegvari A, Benfeitas R, Sperk M, Stahlberg M *et al* (2020) Dysregulation in Akt/mTOR/HIF-1 signaling identified by proteo-transcriptomics of SARS-CoV-2 infected cells. *Emerg Microbes Infect* 9: 1748–1760
- Bailey CC, Kondur HR, Huang IC, Farzan M (2013) Interferon-induced transmembrane protein 3 is a type II transmembrane protein. *J Biol Chem* 288: 32184–32193
- Bailey CC, Zhong G, Huang IC, Farzan M (2014) IFITM-family proteins: the Cell's first line of antiviral defense. *Annu Rev Virol* 1: 261–283
- Barnett KC, Kagan JC (2020) Lipids that directly regulate innate immune signal transduction. *Innate Immun* 26: 4–14
- Batra J, Hultquist JF, Liu D, Shtanko O, Von Dollen J, Satkamp L, Jang GM, Luthra P, Schwarz TM, Small GI *et al* (2018) Protein interaction mapping identifies RBBP6 as a negative regulator of Ebola virus replication. *Cell* 175: e1913
- Brass AL, Huang IC, Benita Y, John SP, Krishnan MN, Feeley EM, Ryan BJ, Weyer JL, van der Weyden L, Fikrig E *et al* (2009) The IFITM proteins

- mediate cellular resistance to influenza A H1N1 virus, West Nile virus, and dengue virus. *Cell* 139: 1243–1254
- Buchrieser J, Degrelle SA, Couderc T, Nevers Q, Disson O, Manet C, Donahue DA, Porrot F, Hillion KH, Perthame E *et al* (2019) IFITM proteins inhibit placental syncytiotrophoblast formation and promote fetal demise. *Science* 365: 176–180
- Chen H, Boutros PC (2011) VennDiagram: a package for the generation of highly-customizable Venn and Euler diagrams in R. *BMC Bioinformatics* 12: 35
- Chesarino NM, McMichael TM, Hach JC, Yount JS (2014a) Phosphorylation of the antiviral protein interferon-inducible transmembrane protein 3 (IFITM3) dually regulates its endocytosis and ubiquitination. *J Biol Chem* 289: 11986–11992
- Chesarino NM, McMichael TM, Yount JS (2014b) Regulation of the trafficking and antiviral activity of IFITM3 by post-translational modifications. *Future Microbiol* 9: 1151–1163
- Compton AA, Bruel T, Porrot F, Mallet A, Sachse M, Euvrard M, Liang C, Casartelli N, Schwartz O (2014) IFITM proteins incorporated into HIV-1 virions impair viral fusion and spread. *Cell Host Microbe* 16: 736–747
- Compton AA, Roy N, Porrot F, Billet A, Casartelli N, Yount JS, Liang C, Schwartz O (2016) Natural mutations in IFITM3 modulate post-translational regulation and toggle antiviral specificity. *EMBO Rep* 17: 1657–1671
- Cox J, Mann M (2008) MaxQuant enables high peptide identification rates, individualized p.p.b.-range mass accuracies and proteome-wide protein quantification. *Nat Biotechnol* 26: 1367–1372
- Coyaud E, Ranadheera C, Cheng D, Goncalves J, Dyakov BJA, Laurent EMN, St-Germain J, Pelletier L, Gingras AC, Brummell JH *et al* (2018) Global Interactomics uncovers extensive organellar targeting by Zika virus. *Mol Cell Proteomics* 17: 2242–2255
- Cureton DK, Massol RH, Saffarian S, Kirchhausen TL, Whelan SP (2009) Vesicular stomatitis virus enters cells through vesicles incompletely coated with clathrin that depend upon Actin for internalization. *PLoS Pathog* 5: e1000394
- Czech MP (2000) PIP2 and PIP3: complex roles at the cell surface. *Cell* 100: 603–606
- Denley A, Gymnopoulos M, Kang S, Mitchell C, Vogt PK (2009) Requirement of phosphatidylinositol(3,4,5)trisphosphate in phosphatidylinositol 3-kinase-induced oncogenic transformation. *Mol Cancer Res* 7: 1132–1138
- Dobin A, Davis CA, Schlesinger F, Drenkow J, Zaleski C, Jha S, Batut P, Chaisson M, Gingeras TR (2013) STAR: ultrafast universal RNA-seq aligner. *Bioinformatics* 29: 15–21
- Dull T, Zufferey R, Kelly M, Mandel RJ, Nguyen M, Trono D, Naldini L (1998) A third-generation lentivirus vector with a conditional packaging system. *J Virol* 72: 8463–8471
- Everitt AR, Clare S, Pertel T, John SP, Wash RS, Smith SE, Chin CR, Feeley EM, Sims JS, Adams DJ *et al* (2012) IFITM3 restricts the morbidity and mortality associated with influenza. *Nature* 484: 519–523
- Fattahi S, Khalifehzadeh-Esfahani Z, Mohammad-Rezaei M, Mafi S, Jafarinia M (2022) PI3K/Akt/mTOR pathway: a potential target for anti-SARS-CoV-2 therapy. *Immunol Res* 70: 269–275
- Follenzi A, Naldini L (2002) Generation of HIV-1 derived lentiviral vectors. *Methods Enzymol* 346: 454–465
- Franz S, Pott F, Zillinger T, Schuler C, Dapa S, Fischer C, Passos V, Stenzel S, Chen F, Dohner K *et al* (2021) Human IFITM3 restricts chikungunya virus and Mayaro virus infection and is susceptible to virus-mediated counteraction. *Life Sci Alliance* 4: e20200909
- Frecha C, Levy C, Costa C, Negre D, Amirache F, Buckland R, Russell SJ, Cosset FL, Verhoeven E (2011) Measles virus glycoprotein-pseudotyped lentiviral vector-mediated gene transfer into quiescent lymphocytes requires binding to both SLAM and CD46 entry receptors. *J Virol* 85: 5975–5985
- Gan X, Wang J, Su B, Wu D (2011) Evidence for direct activation of mTORC2 kinase activity by phosphatidylinositol 3,4,5-trisphosphate. *J Biol Chem* 286: 10998–11002
- Girard-Gagnepain A, Amirache F, Costa C, Levy C, Frecha C, Fusil F, Negre D, Lavillette D, Cosset FL, Verhoeven E (2014) Baboon envelope pseudotyped LVs outperform VSV-G-LVs for gene transfer into early-cytokine-stimulated and resting HSCs. *Blood* 124: 1221–1231
- Gu Z, Eils R, Schlesner M (2016) HilbertCurve: an R/Bioconductor package for high-resolution visualization of genomic data. *Bioinformatics* 32: 2372–2374
- Guo X, Steinkuhler J, Marin M, Li X, Lu W, Dimova R, Melikyan GB (2021) Interferon-induced transmembrane protein 3 blocks fusion of diverse enveloped viruses by altering mechanical properties of cell membranes. *ACS Nano* 15: 8155–8170
- Gurumayum S, Brahma R, Naorem LD, Muthaiyan M, Gopal J, Venkatesan A (2018) ZikaBase: An integrated ZIKV- human interactome map database. *Virology* 514: 203–210
- Harrow J, Frankish A, Gonzalez JM, Tapanari E, Diekhans M, Kokocinski F, Aken BL, Barrell D, Zadissa A, Searle S *et al* (2012) GENCODE: the reference human genome annotation for the ENCODE project. *Genome Res* 22: 1760–1774
- Hosios AM, Wilkinson ME, McNamara MC, Kalafut KC, Torrence ME, Asara JM, Manning BD (2022) mTORC1 regulates a lysosome-dependent adaptive shift in intracellular lipid species. *Nat Metab* 4: 1792–1811
- Hubel P, Urban C, Bergant V, Schneider WM, Knauer B, Stukalov A, Scaturro P, Mann A, Brunotte L, Hoffmann HH *et al* (2019) A protein-interaction network of interferon-stimulated genes extends the innate immune system landscape. *Nat Immunol* 20: 493–502
- Hunter S, Apweiler R, Attwood TK, Bairoch A, Bateman A, Binns D, Bork P, Das U, Daugherty L, Duquenne L *et al* (2009) InterPro: the integrative protein signature database. *Nucleic Acids Res* 37: D211–D215
- Jackson CB, Farzan M, Chen B, Choe H (2022) Mechanisms of SARS-CoV-2 entry into cells. *Nat Rev Mol Cell Biol* 23: 3–20
- John SP, Chin CR, Perreira JM, Feeley EM, Aker AM, Savidis G, Smith SE, Elia AE, Everitt AR, Vora M *et al* (2013) The CD225 domain of IFITM3 is required for both IFITM protein association and inhibition of influenza A virus and dengue virus replication. *J Virol* 87: 7837–7852
- Jones RG, Pearce EJ (2017) mTORing immunity: mTOR signaling in the development and function of tissue-resident immune cells. *Immunity* 46: 730–742
- Kajaste-Rudnitski A, Mashimo T, Frenkiel MP, Guenet JL, Lucas M, Despres P (2006) The 2',5'-oligoadenylate synthetase 1b is a potent inhibitor of West Nile virus replication inside infected cells. *J Biol Chem* 281: 4624–4637
- Kajaste-Rudnitski A, Marelli SS, Pultrone C, Pertel T, Uchil PD, Mechti N, Mothes W, Poli G, Luban J, Vicenzi E (2011) TRIM22 inhibits HIV-1 transcription independently of its E3 ubiquitin ligase activity, tat, and NF-kappaB-responsive long terminal repeat elements. *J Virol* 85: 5183–5196
- Kwofie SK, Schaefer U, Sundararajan VS, Bajic VB, Christoffels A (2011) HCVpro: hepatitis C virus protein interaction database. *Infect Genet Evol* 11: 1971–1977
- Lee WJ, Fu RM, Liang C, Sloan RD (2018) IFITM proteins inhibit HIV-1 protein synthesis. *Sci Rep* 8: 14551
- Lee J, Robinson ME, Ma N, Artadji D, Ahmed MA, Xiao G, Sadras T, Deb G, Winchester J, Cosgun KN *et al* (2020) IFITM3 functions as a PIP3 scaffold to amplify PI3K signalling in B cells. *Nature* 588: 491–497

- Letko M, Marzi A, Munster V (2020) Functional assessment of cell entry and receptor usage for SARS-CoV-2 and other lineage B betacoronaviruses. *Nat Microbiol* 5: 562–569
- Li K, Markosyan RM, Zheng YM, Golfetto O, Bungart B, Li M, Ding S, He Y, Liang C, Lee JC et al (2013) IFITM proteins restrict viral membrane hemifusion. *PLoS Pathog* 9: e1003124
- Li M, Johnson JR, Truong B, Kim G, Weinbren N, Dittmar M, Shah PS, Von Dollen J, Newton BW, Jang GM et al (2019a) Identification of antiviral roles for the exon-junction complex and nonsense-mediated decay in flaviviral infection. *Nat Microbiol* 4: 985–995
- Li N, Zhang YN, Deng CL, Shi PY, Yuan ZM, Zhang B (2019b) Replication-defective West Nile virus with NS1 deletion as a new vaccine platform for flavivirus. *J Virol* 93: e00720-19
- Liao Y, Wang J, Jaehnig EJ, Shi Z, Zhang B (2019) WebGestalt 2019: gene set analysis toolkit with revamped UIs and APIs. *Nucleic Acids Res* 47: W199–W205
- Lin TY, Chin CR, Everitt AR, Clare S, Ferreira JM, Savidis G, Aker AM, John SP, Sarlah D, Carreira EM et al (2013) Amphotericin B increases influenza A virus infection by preventing IFITM3-mediated restriction. *Cell Rep* 5: 895–908
- Ling S, Zhang C, Wang W, Cai X, Yu L, Wu F, Zhang L, Tian C (2016) Combined approaches of EPR and NMR illustrate only one transmembrane helix in the human IFITM3. *Sci Rep* 6: 24029
- Liu P, Gan W, Chin YR, Ogura K, Guo J, Zhang J, Wang B, Blenis J, Cantley LC, Toker A et al (2015) PtdIns(3,4,5)P3-dependent activation of the mTORC2 kinase complex. *Cancer Discov* 5: 1194–1209
- Liu X, Chen L, Fan Y, Hong Y, Yang X, Li Y, Lu J, Lv J, Pan X, Qu F et al (2019) IFITM3 promotes bone metastasis of prostate cancer cells by mediating activation of the TGF-beta signaling pathway. *Cell Death Dis* 10: 517
- Livingstone CD, Barton GJ (1993) Protein sequence alignments: a strategy for the hierarchical analysis of residue conservation. *Comput Appl Biosci* 9: 745–756
- Love MI, Huber W, Anders S (2014) Moderated estimation of fold change and dispersion for RNA-seq data with DESeq2. *Genome Biol* 15: 550
- Lu J, Pan Q, Rong L, He W, Liu SL, Liang C (2011) The IFITM proteins inhibit HIV-1 infection. *J Virol* 85: 2126–2137
- Madiraju C, Novack JP, Reed JC, Matsuzawa SI (2022) K63 ubiquitination in immune signaling. *Trends Immunol* 43: 148–162
- Mairiang D, Zhang H, Sodja A, Murali T, Suriyaphol P, Malasit P, Limjindaporn T, Finley RL Jr (2013) Identification of new protein interactions between dengue fever virus and its hosts, human and mosquito. *PLoS ONE* 8: e53535
- Makvandi-Nejad S, Laurenson-Schafer H, Wang L, Wellington D, Zhao Y, Jin B, Qin L, Kite K, Moghadam HK, Song C et al (2018) Lack of truncated IFITM3 transcripts in cells homozygous for the rs12252-C variant that is associated with severe influenza infection. *J Infect Dis* 217: 257–262
- Matafora V, Corno A, Ciliberto A, Bachi A (2017) Missing value monitoring enhances the robustness in proteomics quantitation. *J Proteome Res* 16: 1719–1727
- Nikoloudis D, Kountouras D, Hiona A (2020) The frequency of combined IFITM3 haplotype involving the reference alleles of both rs12252 and rs34481144 is in line with COVID-19 standardized mortality ratio of ethnic groups in England. *PeerJ* 8: e10402
- Oshlack A, Robinson MD, Young MD (2010) From RNA-seq reads to differential expression results. *Genome Biol* 11: 220
- Ozog S, Timberlake ND, Hermann K, Garijo O, Haworth KG, Shi G, Glinkerman CM, Scheffter LE, D'Souza S, Simpson E et al (2019) Resveratrol trimer enhances gene delivery to hematopoietic stem cells by reducing antiviral restriction at endosomes. *Blood* 134: 1298–1311
- Paunovska K, Da Silva Sanchez A, Foster MT, Loughrey D, Blanchard EL, Islam FZ, Gan Z, Mantalaris A, Santangelo PJ, Dahlman JE (2020) Increased PIP3 activity blocks nanoparticle mRNA delivery. *Sci Adv* 6: eaba5672
- Perreira JM, Chin CR, Feeley EM, Brass AL (2013) IFITMs restrict the replication of multiple pathogenic viruses. *J Mol Biol* 425: 4937–4955
- Petrillo C, Cesana D, Piras F, Bartolaccini S, Naldini L, Montini E, Kajaste-Rudnitski A (2015) Cyclosporin a and rapamycin relieve distinct lentiviral restriction blocks in hematopoietic stem and progenitor cells. *Mol Ther* 23: 352–362
- Petrillo C, Thorne LG, Unali G, Schirotti G, Giordano AMS, Piras F, Cuccovillo I, Petit SJ, Ahsan F, Noursadeghi M et al (2018) Cyclosporine H overcomes innate immune restrictions to improve lentiviral transduction and gene editing in human hematopoietic stem cells. *Cell Stem Cell* 23: e829
- Pia L, Rowland-Jones S (2022) Omicron entry route. *Nat Rev Immunol* 22: 144
- Pichlmair A, Kandasamy K, Alvisi G, Mulhern O, Sacco R, Habjan M, Binder M, Stefanovic A, Eberle CA, Goncalves A et al (2012) Viral immune modulators perturb the human molecular network by common and unique strategies. *Nature* 487: 486–490
- Platanias LC (2005) Mechanisms of type-I- and type-II-interferon-mediated signalling. *Nat Rev Immunol* 5: 375–386
- Plattet P, Alves L, Herren M, Aguilar HC (2016) Measles virus fusion protein: structure, function and inhibition. *Viruses* 8: 112
- Prelli Bozzo C, Nchioua R, Volcic M, Koepke L, Kruger J, Schutz D, Heller S, Sturzel CM, Kmiec D, Conzelmann C et al (2021) IFITM proteins promote SARS-CoV-2 infection and are targets for virus inhibition in vitro. *Nat Commun* 12: 4584
- Rahman K, Coomer CA, Majdoul S, Ding SY, Padilla-Parra S, Compton AA (2020) Homology-guided identification of a conserved motif linking the antiviral functions of IFITM3 to its oligomeric state. *Elife* 9: e58537
- Rajapaksa US, Jin C, Dong T (2020) Malignancy and IFITM3: friend or foe? *Front Oncol* 10: 593245
- Randolph AG, Yip WK, Allen EK, Rosenberger CM, Agan AA, Ash SA, Zhang Y, Bhangale TR, Finkelstein D, Cvijanovich NZ et al (2017) Evaluation of IFITM3 rs12252 association with severe pediatric influenza infection. *J Infect Dis* 216: 14–21
- Rappsilber J, Ishihama Y, Mann M (2003) Stop and go extraction tips for matrix-assisted laser desorption/ionization, nanoelectrospray, and LC/MS sample pretreatment in proteomics. *Anal Chem* 75: 663–670
- Santa Cruz Garcia AB, Schnur KP, Malik AB, Mo GCH (2022) Gasdermin D pores are dynamically regulated by local phosphoinositide circuitry. *Nat Commun* 13: 52
- Scialo F, Daniele A, Amato F, Pastore L, Matera MG, Cazzola M, Castaldo G, Bianco A (2020) ACE2: the major cell entry receptor for SARS-CoV-2. *Lung* 198: 867–877
- Shannon P, Markiel A, Ozier O, Baliga NS, Wang JT, Ramage D, Amin N, Schwikowski B, Ideker T (2003) Cytoscape: a software environment for integrated models of biomolecular interaction networks. *Genome Res* 13: 2498–2504
- Shi G, Ozog S, Torbett BE, Compton AA (2018) mTOR inhibitors lower an intrinsic barrier to virus infection mediated by IFITM3. *Proc Natl Acad Sci USA* 115: E10069–E10078
- Shi G, Kenney AD, Kudryashova E, Zani A, Zhang L, Lai KK, Hall-Stoodley L, Robinson RT, Kudryashov DS, Compton AA et al (2021) Opposing activities of IFITM proteins in SARS-CoV-2 infection. *EMBO J* 40: e106501
- Sievers F, Wilm A, Dineen D, Gibson TJ, Karplus K, Li W, Lopez R, McWilliam H, Remmert M, Soding J et al (2011) Fast, scalable generation of high-

- quality protein multiple sequence alignments using Clustal omega. *Mol Syst Biol* 7: 539
- Smith S, Weston S, Kellam P, Marsh M (2014) IFITM proteins-cellular inhibitors of viral entry. *Curr Opin Virol* 4: 71–77
- Spence JS, He R, Hoffmann HH, Das T, Thinon E, Rice CM, Peng T, Chandran K, Hang HC (2019) IFITM3 directly engages and shuttles incoming virus particles to lysosomes. *Nat Chem Biol* 15: 259–268
- Suddala KC, Lee CC, Meraner P, Marin M, Markosyan RM, Desai TM, Cohen FS, Brass AL, Melikyan GB (2019) Interferon-induced transmembrane protein 3 blocks fusion of sensitive but not resistant viruses by partitioning into virus-carrying endosomes. *PLoS Pathog* 15: e1007532
- Sun F, Xia Z, Han Y, Gao M, Wang L, Wu Y, Sabatier JM, Miao L, Cao Z (2020) Topology, antiviral functional residues and mechanism of IFITM1. *Viruses* 12: 295
- Tartour K, Nguyen XN, Appourchoux R, Assil S, Barateau V, Bloyet LM, Burlaud Gaillard J, Confort MP, Escudero-Perez B, Gruffat H et al (2017) Interference with the production of infectious viral particles and bimodal inhibition of replication are broadly conserved antiviral properties of IFITMs. *PLoS Pathog* 13: e1006610
- Tian J, Zhang X, Wu H, Liu C, Li Z, Hu X, Su S, Wang LF, Qu L (2015) Blocking the PI3K/AKT pathway enhances mammalian reovirus replication by repressing IFN-stimulated genes. *Front Microbiol* 6: 886
- Tripathi S, Pohl MO, Zhou Y, Rodriguez-Frandsen A, Wang G, Stein DA, Moulton HM, DeJesus P, Che J, Mulder LC et al (2015) Meta- and orthogonal integration of influenza “OMICs” data defines a role for UBR4 in virus budding. *Cell Host Microbe* 18: 723–735
- Tyanova S, Temu T, Sinitcyn P, Carlson A, Hein MY, Geiger T, Mann M, Cox J (2016) The Perseus computational platform for comprehensive analysis of (prote)omics data. *Nat Methods* 13: 731–740
- Unali G, Giordano AMS, Cuccovillo I, Alezz MA, Apolonia L, Merelli I, Malim MH, Petrillo C, Kajaste-Rudnitski A (2021) The lysine-rich intracellular loop and cell type-specific co-factors are required for IFITM3 antiviral immunity in hematopoietic stem cells. *bioRxiv* <https://doi.org/10.1101/2021.04.06.438585> [PREPRINT]
- Vanhaesebroeck B, Guillermet-Guibert J, Graupera M, Bilanges B (2010) The emerging mechanisms of isoform-specific PI3K signalling. *Nat Rev Mol Cell Biol* 11: 329–341
- Wang CX, Sather BD, Wang X, Adair J, Khan I, Singh S, Lang S, Adams A, Curinga G, Kiem HP et al (2014) Rapamycin relieves lentiviral vector transduction resistance in human and mouse hematopoietic stem cells. *Blood* 124: 913–923
- Wang L, Fu B, Li W, Patil G, Liu L, Dorf ME, Li S (2017) Comparative influenza protein interactomes identify the role of plakophilin 2 in virus restriction. *Nat Commun* 8: 13876
- Waterhouse AM, Procter JB, Martin DM, Clamp M, Barton GJ (2009) Jalview version 2—a multiple sequence alignment editor and analysis workbench. *Bioinformatics* 25: 1189–1191
- Winstone H, Lista MJ, Reid AC, Bouton C, Pickering S, Galao RP, Kerridge C, Doores KJ, Swanson CM, Neil SJD (2021) The polybasic cleavage site in SARS-CoV-2 spike modulates viral sensitivity to type I interferon and IFITM2. *J Virol* 95: e02422-20
- Wu T, Hu E, Xu S, Chen M, Guo P, Dai Z, Feng T, Zhou L, Tang W, Zhan L et al (2021) clusterProfiler 4.0: a universal enrichment tool for interpreting omics data. *Innovation (Camb)* 2: 100141
- Xu-Yang Z, Pei-Yu B, Chuan-Tao Y, Wei Y, Hong-Wei M, Kang T, Chun-Mei Z, Ying-Feng L, Xin W, Ping-Zhong W et al (2016) Interferon-induced transmembrane protein 3 inhibits Hantaan virus infection, and its single nucleotide polymorphism rs12252 influences the severity of hemorrhagic fever with renal syndrome. *Front Immunol* 7: 535
- Yount JS, Karssemeijer RA, Hang HC (2012) S-palmitoylation and ubiquitination differentially regulate interferon-induced transmembrane protein 3 (IFITM3)-mediated resistance to influenza virus. *J Biol Chem* 287: 19631–19641
- Yu J, Li M, Wilkins J, Ding S, Swartz TH, Esposito AM, Zheng YM, Freed EO, Liang C, Chen BK et al (2015) IFITM proteins restrict HIV-1 infection by antagonizing the envelope glycoprotein. *Cell Rep* 13: 145–156
- Zang R, Case JB, Yutuc E, Ma X, Shen S, Gomez Castro MF, Liu Z, Zeng Q, Zhao H, Son J et al (2020) Cholesterol 25-hydroxylase suppresses SARS-CoV-2 replication by blocking membrane fusion. *Proc Natl Acad Sci USA* 117: 32105–32113
- Zhang Y, Qin L, Zhao Y, Zhang P, Xu B, Li K, Liang L, Zhang C, Dai Y, Feng Y et al (2020) Interferon-induced transmembrane protein 3 genetic variant rs12252-C associated with disease severity in coronavirus disease 2019. *J Infect Dis* 222: 34–37
- Zhao X, Li J, Winkler CA, An P, Guo JT (2018a) IFITM genes, variants, and their roles in the control and pathogenesis of viral infections. *Front Microbiol* 9: 3228
- Zhao X, Sehgal M, Hou Z, Cheng J, Shu S, Wu S, Guo F, Le Marchand SJ, Lin H, Chang J et al (2018b) Identification of residues controlling restriction versus enhancing activities of IFITM proteins on entry of human coronaviruses. *J Virol* 92: e01535-17
- Zhao H, Lu L, Peng Z, Chen LL, Meng X, Zhang C, Ip JD, Chan WM, Chu AW, Chan KH et al (2022) SARS-CoV-2 omicron variant shows less efficient replication and fusion activity when compared with Delta variant in TMPRSS2-expressed cells. *Emerg Microbes Infect* 11: 277–283
- Zhong L, Uzbekov R, Journo C, Roingard P, Cimarelli A (2021) A novel domain within the CIL regulates egress of IFITM3 from the Golgi and prevents its deleterious accumulation in this apparatus. *bioRxiv* <https://doi.org/10.1101/2021.03.29.437470> [PREPRINT]



License: This is an open access article under the terms of the [Creative Commons Attribution-NonCommercial-NoDerivs](https://creativecommons.org/licenses/by-nc-nd/4.0/) License, which permits use and distribution in any medium, provided the original work is properly cited, the use is non-commercial and no modifications or adaptations are made.

Expanded View Figures

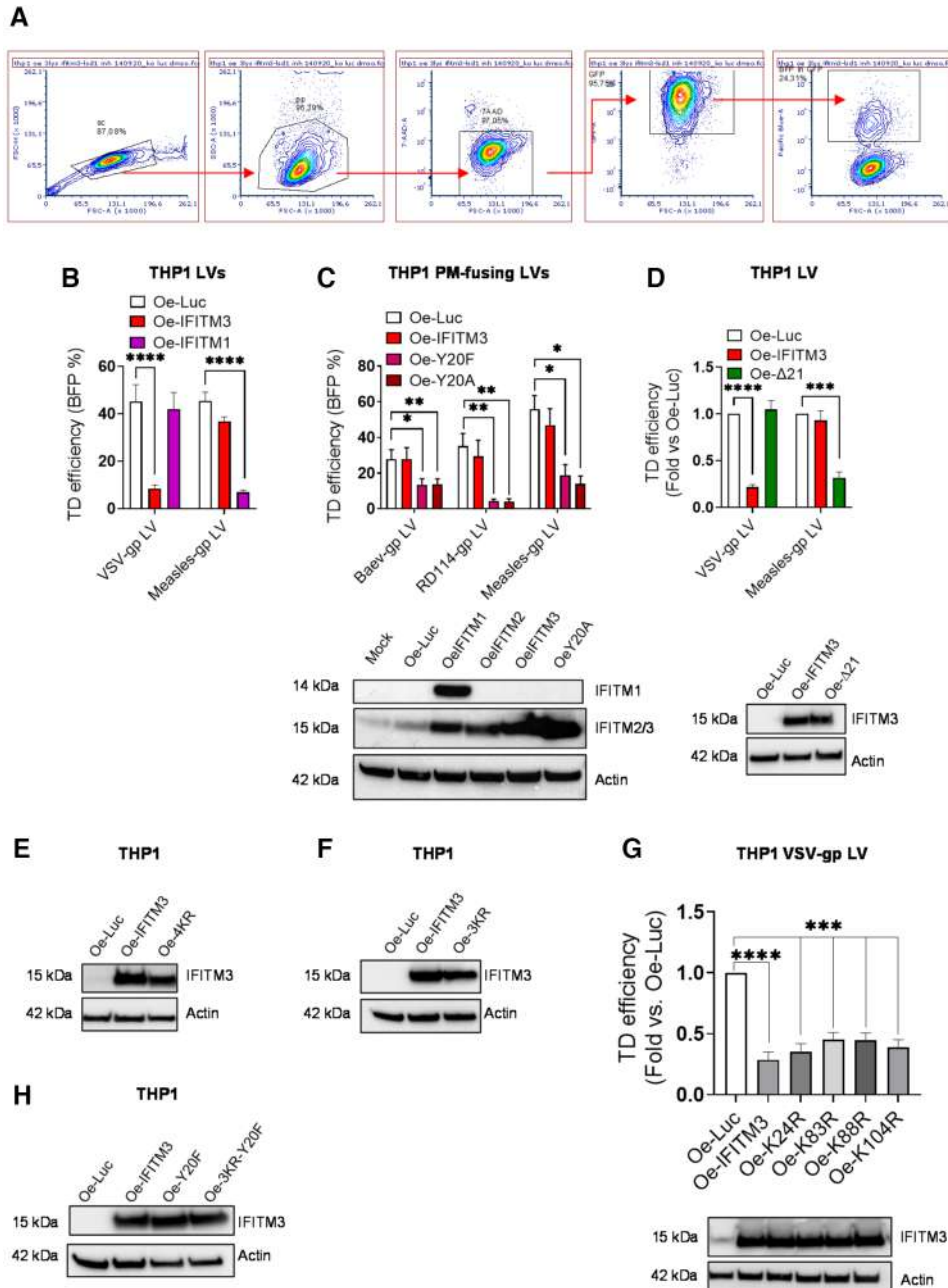


Figure EV1.

Figure EV1. IFITM1, IFITM3, and single lysine IFITM3 target different viral entry routes depending on their cellular localization.

- A Gating strategy for acquisition of transduction efficiencies in the different cell lines.
- B THP1 overexpressing (Oe) IFITM3, IFITM1, or control were transduced with VSV-gp or measles-gp-pseudotyped LVs at MOI 1 (mean \pm SEM, $n > 6$ biological replicates run in technical duplicate), transduction efficiency was measured by flow cytometry 5-day post-TD as % of BFP⁺ cells. P -values are for Mann–Whitney test, ****for $P < 0.0001$.
- C THP1 overexpressing IFITM3 wild-type, IFITM3 PM-confined mutants or control were transduced at MOI 1 with PM-fusing LVs (mean \pm SEM, $n > 5$ biological replicates run in technical duplicate), P -values are for Mann–Whitney test, * for $P < 0.05$, **for $P < 0.01$. IFITM1, IFITM2, IFITM3, Y20F, and Y20A overexpression was confirmed by WB in THP1.
- D THP1 overexpressing the putative IFITM3 isoform ($\Delta 21$) encoded by the SNP rs-1225-C or control were transduced with either VSV-gp or measles-gp-pseudotyped LVs. Transduction efficiency was measured 5 days later (mean \pm SEM, $n = 5$ biological replicates run in technical duplicate), P -values are for one-sample t -test, *** for $P < 0.001$, **** for $P < 0.0001$. IFITM3-WT and IFITM3- $\Delta 21$ overexpression was confirmed by WB in THP1.
- E, F IFITM3 protein expression was evaluated by WB at time of TD in THP1 overexpressing IFITM3, IFITM3-4KR, or IFITM3-3KR.
- G THP1 overexpressing single lysine mutants IFITM3 or control were transduced with VSV-gp-pseudotyped LV. Transduction efficiency was measured by flow cytometry 5-day post-TD (mean \pm SEM, $n = 6$ biological replicates run in technical duplicate). Overexpression was confirmed by WB at the time of TD. P -values are for one-sample t -test versus Oe-Luc = 1. *** for $P < 0.001$, **** for $P < 0.0001$.
- H THP1 overexpressing IFITM3, IFITM3-Y20F, IFITM3-Y20F-3KR, or control were validated by WB.

Source data are available online for this figure.

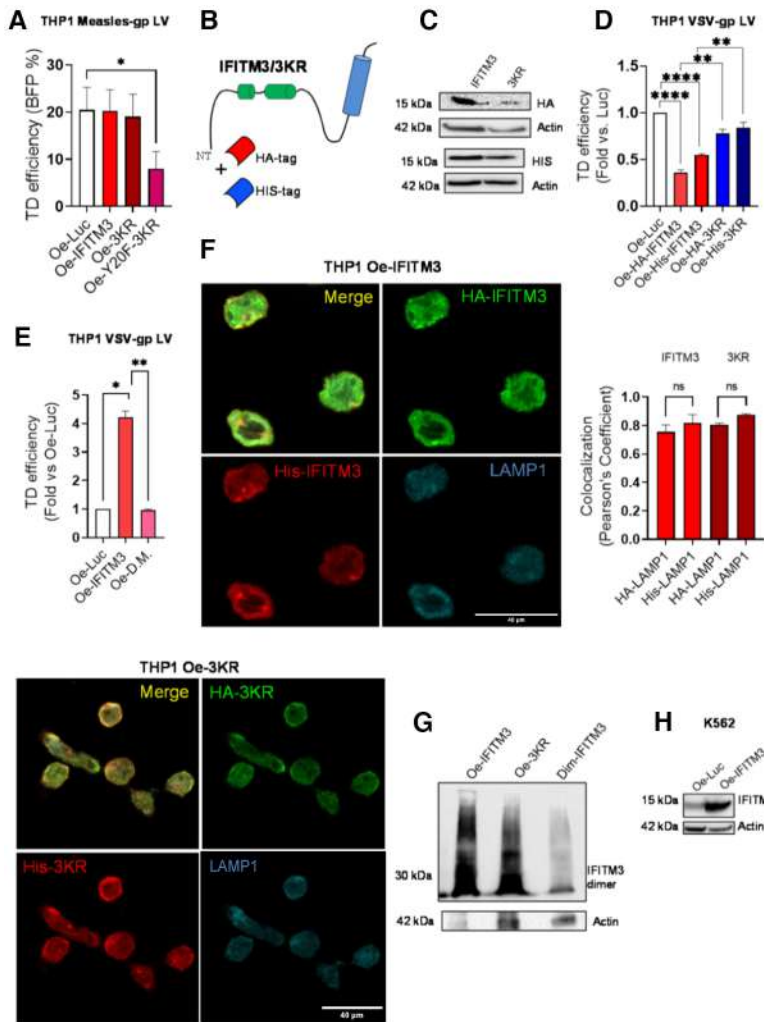


Figure EV2. IFITM3 loss of antiviral activity is localization and dimerization independent.

- A THP1 overexpressing IFITM3, IFITM3-3KR, IFITM3-Y20F-3KR, or control were transduced with measles-gp-pseudotyped LV. Transduction efficiency was evaluated 5-day post-TD (mean ± SEM, *n* = 3 biological replicates run in technical duplicate). *P*-values are for one paired *t*-test. * for *P* < 0.05.
- B Schematic representation of IFITM3 wild-type or 3KR mutant tagged with hemagglutinin (HA) or Histidine at the N terminus (NT).
- C Overexpression of IFITM3-tagged constructs was validated in THP1 by WB.
- D THP1 overexpressing tagged IFITM3, tagged IFITM3-3KR or control were transduced with VSV-gp-pseudotyped LV. Transduction was evaluated 5-day post-TD (mean ± SEM, *n* = 6 biological replicates run in technical duplicate). *P*-values are for one-sample *t*-test versus Oe-Luc = 1 for comparisons with tagged IFITM3 or Mann-Whitney test for comparisons between tagged IFITM3 and tagged IFITM3-3KR. ** for *P* < 0.01, **** for *P* < 0.0001.
- E THP1 overexpressing tagged IFITM3, tagged IFITM3-dimer mutant or control were transduced with VSV-gp-pseudotyped LV. Transduction was evaluated 5-day post-TD (mean ± SEM, *n* = 6 biological replicates run in technical duplicate). *P*-values are for one-sample *t*-test versus Oe-Luc = 1 for comparisons with tagged IFITM3 or Mann-Whitney test for comparisons between tagged IFITM3 and tagged IFITM3-dimer mutant. * for *P* < 0.05, ** for *P* < 0.01.
- F HA-IFITM3, His-IFITM3, HA-3KR, His-3KR, and Lamp1 levels were measured by immunofluorescence (mean ± SEM, *n* = 3 biological replicates; zoomed images are shown, scale bar 40 μm). The Pearson's correlation coefficient of HA, His, and Lamp1 colocalization of three independent biological experiments was calculated. *P*-values are for Mann-Whitney test. ns for not significant.
- G IFITM3 dimerization was assessed by native PAGE followed by WB analysis in THP1 (*n* = 4 biological replicates).
- H IFITM3 overexpression was confirmed in K562 at the time of TD.

Source data are available online for this figure.

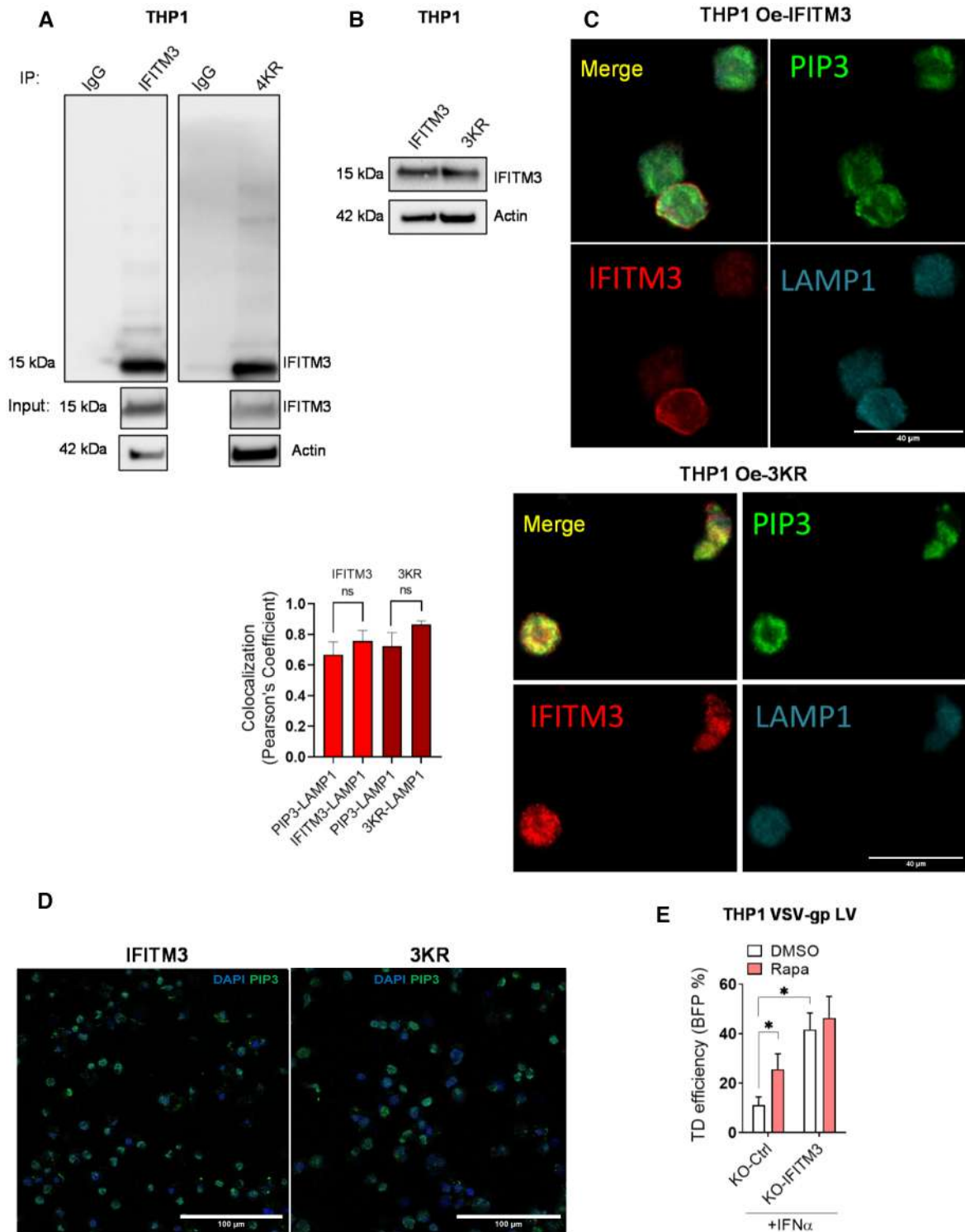


Figure EV3.

Figure EV3. IFITM3 requires interaction with PIP3 for its antiviral activity.

- A IFITM3 wild-type or IFITM3-4KR immunoprecipitations were confirmed by WB.
- B IFITM3 wild-type or IFITM3-3KR expression levels were measured in THP1 KO for endogenous IFITM3.
- C IFITM3 and PIP3 colocalization with LAMP1 was evaluated by immunofluorescence. Representative zoomed images are shown (mean \pm SEM, $n = 3$ biological replicates), scale bar 40 μ m. The Pearson's correlation coefficient of HA, His, and Lamp1 colocalization of three independent biological experiments was calculated. ns for not significant.
- D Total PIP3 was quantified by IF in THP1 cells overexpressing the double-tagged His/HA IFITM3 wild-type or IFITM3-3KR. Representative images are shown.
- E THP1 KO for IFITM3 or control were stimulated with IFN α for 24 h and then transduced with VSV-gp-pseudotyped LV in the presence or absence of Rapamycin. Transduction levels were measured 5 days after TD (mean \pm SEM, $n = 6$ biological replicates run in technical duplicate). *P*-values are for Wilcoxon test, * for $P < 0.05$.

Source data are available online for this figure.

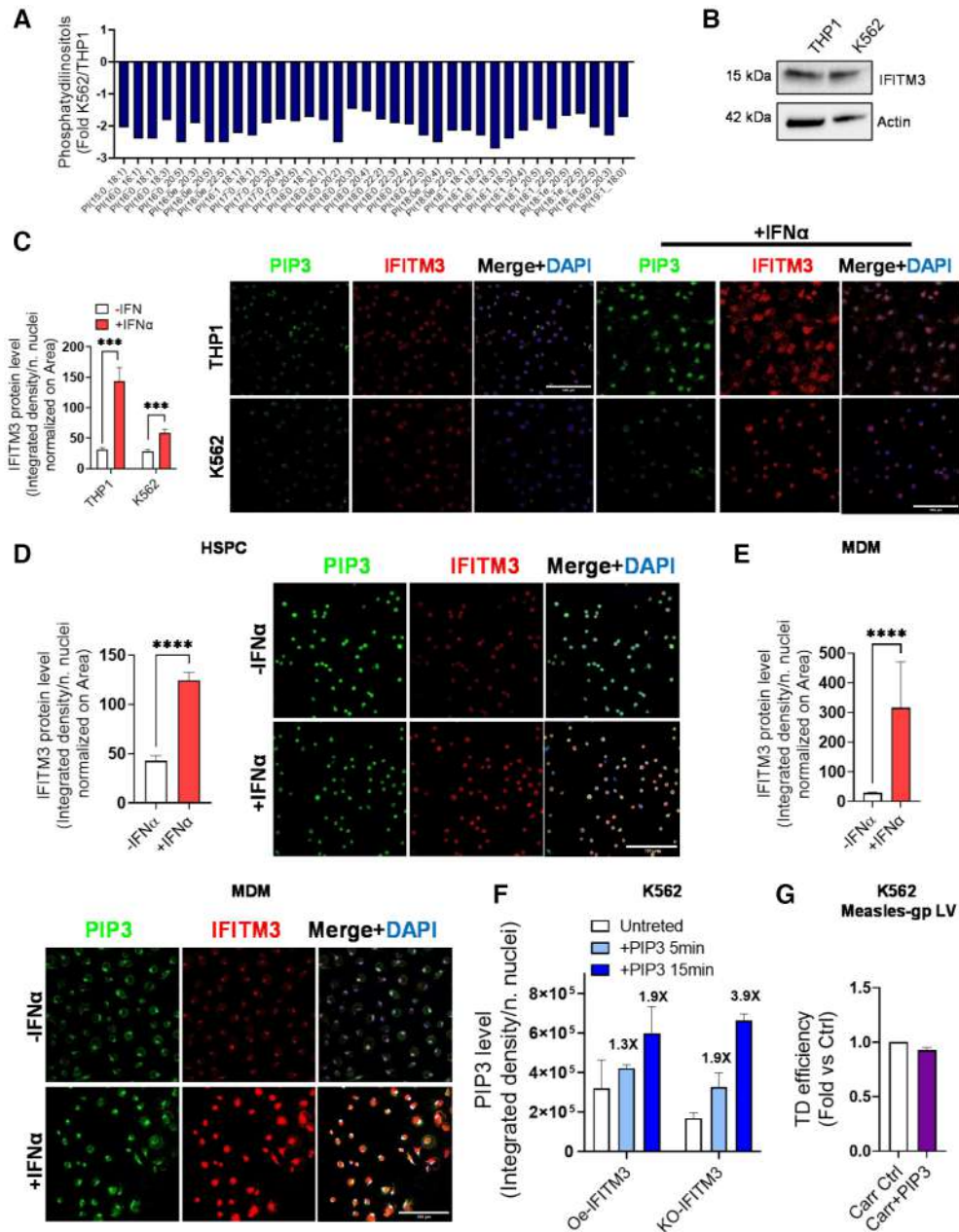


Figure EV4.

Figure EV4. PIP3 is an interferon-inducible phospholipid.

- A All Phosphatidylinositol (PI) species were measured in K562 and THP1. Log plots of PI ratio in K562 versus THP1 are shown.
- B IFITM3 expression was evaluated by WB in THP1 and K562 cells KO for endogenous IFITM3 and overexpressing IFITM3.
- C–E PIP3 levels were measured by immunofluorescence in THP1 and K562 (C), HSPC (D) and MDM (E) prestimulated with IFN α . (mean \pm SEM, $n = 3$ biological replicates). P -values are for Mann–Whitney test, * for $P < 0.05$. Representative images are shown, scale bar 100 μ m.
- F K562 were provided of exogenous PIP3 or Carr Ctrl alone. Successful PIP3 intake was verified by IF 5 and 15-min postdelivery by IF ($n = 8$ acquired from two independent biological experiments).
- G K562 were provided of exogenous PIP3 or Carr Ctrl alone and then transduced with measles-gp-pseudotyped LV. Transduction was measured 5 days later (mean \pm SEM, $n = 4$ biological replicates run in duplicate).

Source data are available online for this figure.

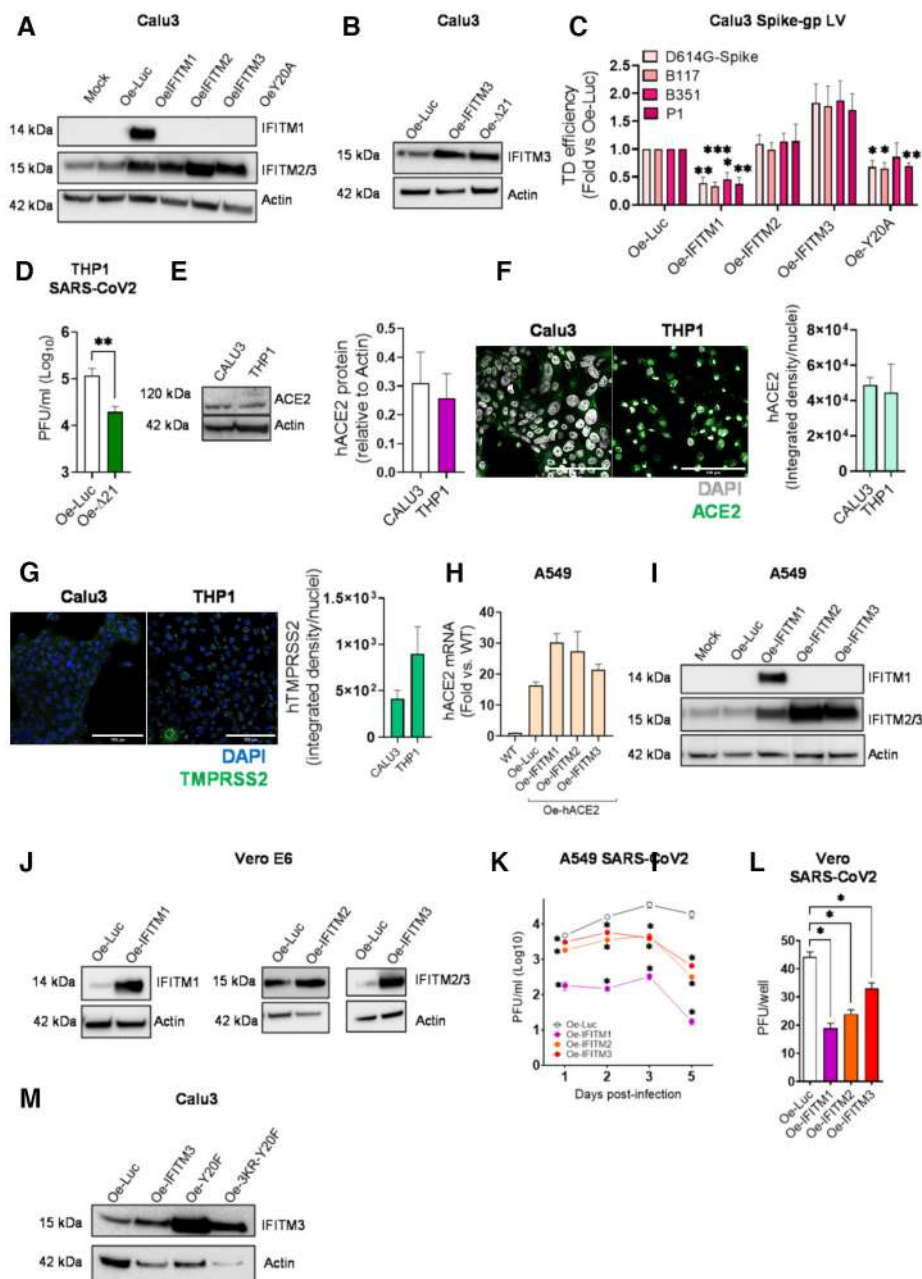


Figure EV5.

Figure EV5. IFITM1 blocks entry of SARS-CoV2 in Calu3 and THP1.

- A Overexpression of IFITM1, IFITM2, IFITM3, and IFITM3-Y20A was verified by WB in Calu3.
- B IFITM3-WT and IFITM3-Δ21 overexpression was confirmed by WB in Calu3.
- C Calu3 overexpressing IFITM1, IFITM2, IFITM3, IFITM3-Y20A mutant, and control were transduced with LV-pseudotyped with different Spike variants. Error bars are presented as mean ± SEM ($n = 6$ biological replicates run in duplicate); P -values are for one-sample t -test, * for $P < 0.05$, ** for $P < 0.01$, *** for $P < 0.001$.
- D THP1 overexpressing Δ21-IFITM3 or control were infected with SARS CoV2 for 3 days. Viral titer was assessed by plaque assay in Vero E6 cells (mean ± SEM, $n = 4$ biological replicates run in technical triplicate). P -values are for Mann–Whitney test, ** for $P < 0.01$.
- E ACE2 protein level was measured in Calu2 and THP1. Quantification was performed by ImageJ over the normalizer (mean ± SEM, $n = 5$ biological replicates).
- F, G Human Ace2 (F) and TMPRSS2 (G) expression at the cell surface was analyzed in Calu3 and THP1 cells by immunofluorescence. Protein quantification was performed using ImageJ software (mean ± SEM, $n = 4–3$ biological replicates); representative images are shown ($n = 12–6$ images), scale bar 100 μm.
- H A549 overexpressing ACE2 was validated by RT–qPCR. (mean ± SEM, $n = 3$ biological replicates).
- I, J Overexpression of IFITM1, IFITM2, or IFITM3 was measured in A549 (I) or Vero E6 cells (J).
- K A549 cells overexpressing IFITM1, IFITM2, IFITM3, or control were infected with SARS-CoV2 at MOI 1. Viral supernatants were collected at different time points and tittered on Vero E6 cells. Data are presented as mean ± SEM ($n = 4$ biological replicates run in technical duplicate). P -values are for Mann–Whitney test, * $P < 0.05$.
- L Vero E6 cells overexpressing IFITM1, IFITM2, IFITM3, or control were infected with SARS-CoV2 at MOI 1. Titers were calculated through direct plaque assay 72-h postinfection. ($n = 3$ biological replicates run in technical duplicate). P -values are for Mann–Whitney test, * $P < 0.05$.
- M Calu3 overexpressing IFITM3, IFITM3-Y20F, IFITM3-Y20F-3KR, or control was validated by WB.

Source data are available online for this figure.